GENERAL ATOMIC

GA-A14161

GAMMA SCANNING THE PRIMARY CIRCUIT OF THE PEACH BOTTOM HTGR

by
D. L. HANSON, N. L. BALDWIN, and W. E. SELPH*

This is a preprint of a paper to be presented at the
American Nuclear Society/European Nuclear Society
1976 International Meeting, Washington, D.C.,
November 14-19, 1976

Work supported by
Contract E(04-3)-167
Project Agreement No. 56
U.S. Energy Research and Development Administration
and the Electric Power Research Institute

*Intelcom Rad Tech Corporation, San Diego, California

GENERAL ATOMIC PROJECT 3238

OCTOBER 1976

DISCLAIMER

ABSTRACT

The plateout distribution of gamma-emitting nuclides in the primary circuit of the Peach Bottom HTGR at end-of-life has been determined by in situ gamma scanning. Part of the Peach Bottom End-of-Life Program, the work was performed by IRT Corporation under subcontract to General Atomic. The measurements were made to test the validity of fission product transport predictions. The specific activity was mapped by scanning the accessible ducting at 12 locations with a Ge(Li) detector and by axially traversing 79 steam generator tubes with travelling CdTe detectors from the water side. Following destructive removal of trepan samples, a travelling intrinsic germanium detector was inserted sequentially into two vertical ducts and the plateout mapped along 6-m runs of ducting. Calibration measurements on mockups allowed reduction of the spectra to specific activity. The measured plateout profiles were in excellent agreement with those predicted with the PAD code.

The external duct scans were straightforward; ORNL had made similar measurements throughout Core 2 operation. Mapping the plateout activity on the tube bundle was more formidable in that the steam generator tubes, some with a 9.6-mm inside diameter, had to be traversed to a depth of 6 m. A miniaturized, tantalum-shielded, cadmium telluride semiconductor detector was found acceptable. With access at the tubesheet, the detector affixed to a coaxial cable was inserted to the bottom of the U-tube, and spectra were acquired at 0.15-m increments as the detector was withdrawn remotely. A similar configuration for transporting the germanium detector was used for the internal duct scans.

The dominant gamma emitters were Cs-137 and Cs-134; their relative distributions were similar. Little local structure to the plateout in the ducts was observed, only a gradual decrease in specific activity in the direction

of coolant flow. In the steam generator, a significant entrance effect was observed in the superheater section; the activity was highest where the inlet jet impinged and lowest at the ends of the bundle despite the presence of a flow baffle. The effect damped out with penetration into the bundle, and the axial profile was uniform at the economizer exit. When the axial profiles are averaged, the specific activity decreased monotonically across the tube bundle.

Cesium deposition throughout the circuit was apparently mass transfer controlled with the exception of the hot duct where the accumulation was limited by the high temperatures. The superheater entrance effect probably resulted from the maldistribution of coolant flow. The profiles suggest that cesium was transported primarily in atomic form despite the presence of carbonaceous dust. Finally, the measured plateout distribution verifies the reference methodology used to make such predictions for large HTGR design.

CONTENTS

FIGURES

TABLES

1. INTRODUCTION

The plateout distribution of radionuclides in the primary circuit of the Peach Bottom HTGR has been determined to test the validity of fission product transport predictions; the work is part of the Peach Bottom End-of-Life Program (Ref. 1) jointly sponsored by the Energy Research and Development Administration and the Electric Power Research Institute. The specific plateout activities have been determined by a combination of *in situ* gamma scanning and radiochemical analysis of samples destructively removed from circuit components. The *in situ* circuit scans were performed by IRT Corporation, San Diego, Ca., under subcontract to GA. Data reduction is essentially complete with the exception of final confirmation of the calibration technique. It is the purpose of this discussion to summarize and evaluate these measurements and, in particular, to compare the measured plateout distributions with those predicted with the PAD code (Ref. 2).

The purpose of the circuit gamma scanning was to measure the amount and distribution of plateout activity in order to: (1) test the validity of plateout models and predictions, (2) test the validity of total core release predictions (by integration of the plateout distribution), and (3) complement and complete on-going surveillance programs which monitored plateout levels throughout Core 2 operation. The work was accomplished in two phases. The essential features were established in the test specifications (Refs. 3, 4), the methodology was described in the test procedures (Refs. 5, 6), and the results were documented in the data compilation report (Ref. 7). The use of these data for code validation is developed in the design methods verification work plan (Ref. 8).

1.1 REACTOR DESCRIPTION

A complete description of the Peach Bottom High-Temperature Gas-Cooled Reactor (HTGR) is given in the Final Hazards Summary Report (Ref. 9), and a

concise description is given in Ref. 10; both documents are exerpted below. The Peach Bottom primary circuit is shown schematically in Fig. 1. The cold helium coolant at 23.8 atm and 330°C enters the upflow core where it is heated to a nominal gas outlet temperature of about 700°C. Upon exit from the upper core plenum, the coolant flow is split between two parallel loops. The hot helium is directed toward the steam generators through the inner pipe of a concentric duct; the thermal barrier of the hot duct consists of panels of honeycomb insulation and staggered cover plates, both of 304 stainless steel. Hot helium enters the vertical U-tube steam generator (shown in Fig. 2) making a single horizontal pass across the superheater, evaporator, and economizer tubes; a vertical impingement-baffle and horizontal tube support baffles are designed to distribute the flow uniformly along the vertical length of the bundle. The tube bundle shroud is also lined on the hot gas side with honeycomb insulation.

Each coolant loop contains a bypass dust collector for removal of particulate matter; these filters are in parallel with the helium circulators. Approximately 1% of the total recirculating helium flow from the circulators passes through the dust filters. Being inertial devices, these separators remove effectively only those particles which are several microns or larger in diameter.

Owned and operated by the Philadelphia Electric Company, the Peach Bottom HTGR operated for over 7 years with final shutdown for decommissioning on October 31, 1974. Core 1 operation was terminated prematurely at 452 effective full power days (EFPD) because of fuel element sleeve failure. Core 2 achieved full burnup of 897 EFPD. An operating history report summarizing the Peach Bottom operating experience in detail has been prepared (Ref. 11).

1.2 PEACH BOTTOM PRIMARY CIRCUIT GAMMA SCANNING

1.2.1 ORNL Operational Surveillance

Personnel from ORNL (J. deNordwall, F. Dyer, et al.) made periodic gamma scans of accessible ducting throughout Core 2 operation as part of

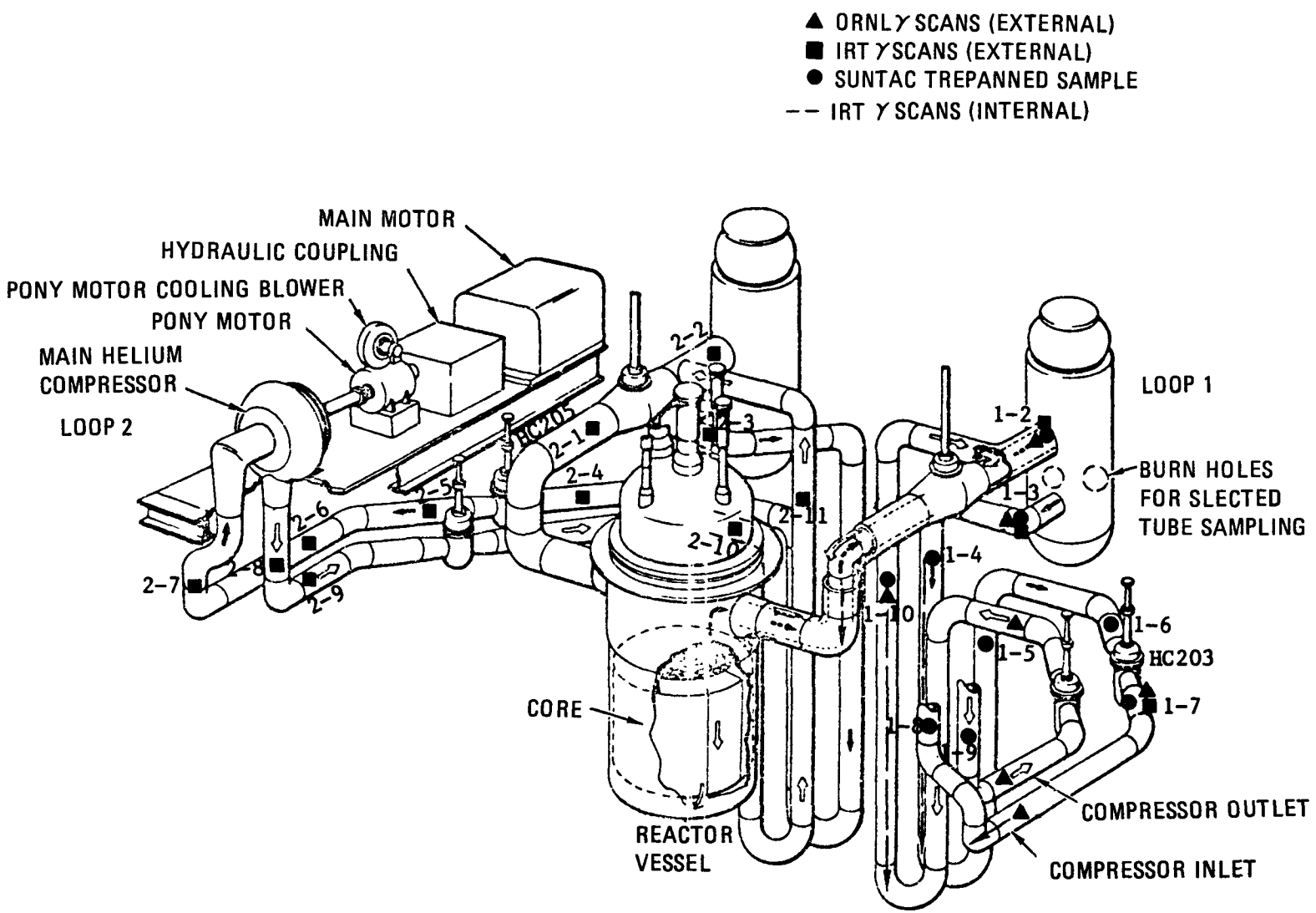

Fig. 1. Isometric of primary coolant system

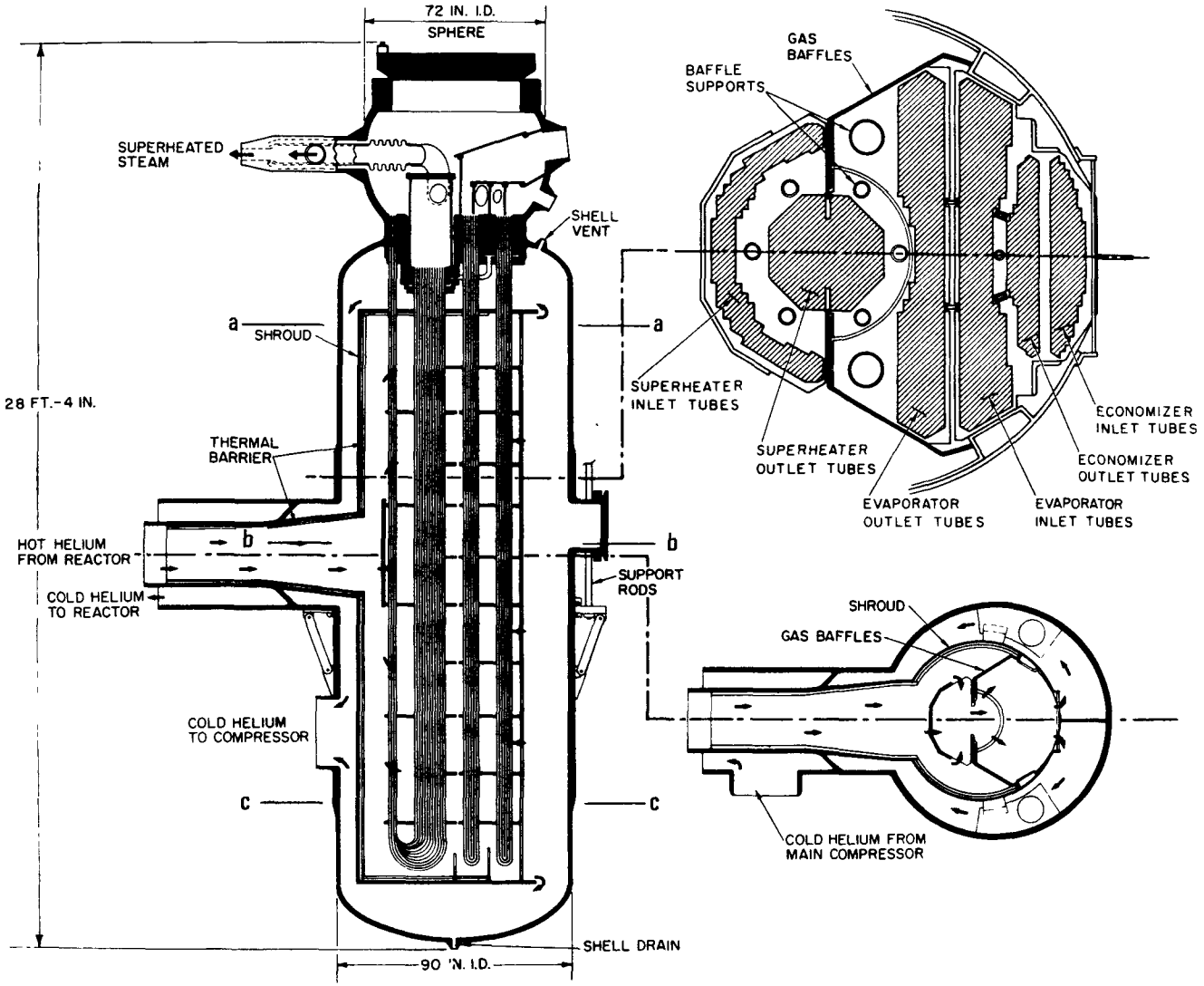

Fig. 2. Cross section of steam generator

their operational surveillance program; their scanning locations are indicated by triangles in Fig. 1. Results of their work are included in a coolant chemistry report (Ref. 12). Although the ORNL measurements are concentrated in one portion of the circuit (the cold ducting of loop 1), they are invaluable in that they provide the most accurate time history of the plateout activity (hence, core release).

1.2.2 IRT Circuit Gamma Scanning

The purpose of the IRT work was to map completely the end-of-life plateout activity in the circuit within the constraints imposed by budget and schedule limitations as well as current detector technology. Gamma scanning the accessible ducting was a straightforward extension of the scanning work which had been done by ORNL. However, a substantial fraction of the plateout inventory was expected to be in the steam generator, and mapping the activity on the tube bundle was more formidable in that the tubes, some with a 9.6-mm inside diameter, had to be traversed to a depth of ~6 m. IRT suggested that a miniaturized cadmium telluride detector could be adapted for the tube scanning and hence their involvement in the Peach Bottom End-of-Life Program.

The IRT circuit gamma scanning work was divided into two phases. The first and major phase of the work consisted of scanning the hot and cold ducting at 12 locations with a lithium-drifted germanium detector and of axially traversing 79 steam generator tubes with travelling CdTe detectors from the water side. In the second phase, which followed removal of trepan samples, a travelling intrinsic germanium detector was inserted sequentially into two vertical ducts, and the gamma activity was mapped along approximately 6-m straight runs of ducting. The duct scanning locations are shown in Fig. 1. Those steam generator tubes which were scanned are indicated on the tube field shown in Fig. 3. The gamma spectra obtained at Peach Bottom were reduced to specific activity by calibration measurements which were made on laboratory mockups.

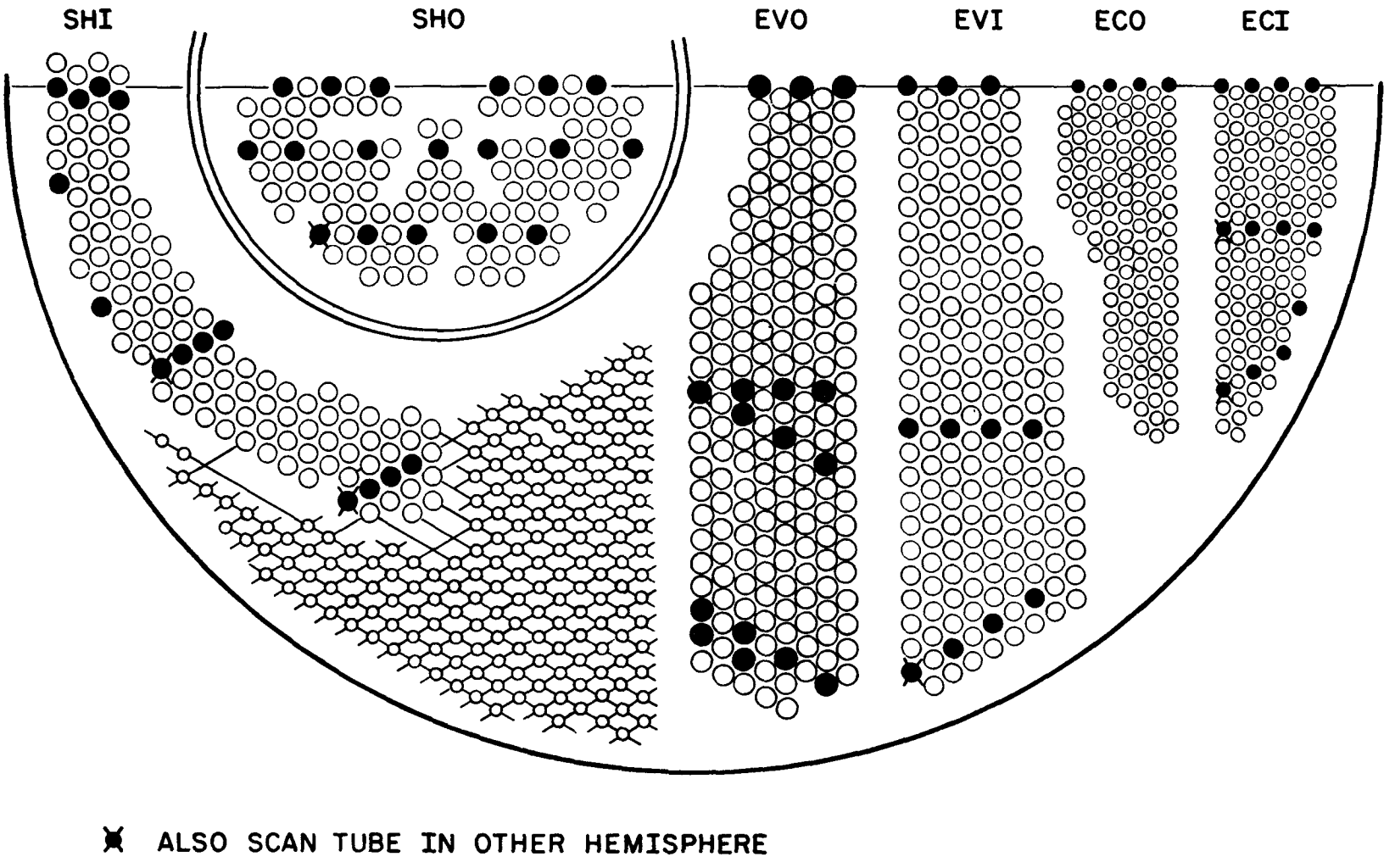

Fig. 3. Steam generator tube γ-scan locations

1.3 PREDICTION OF THE PLATEOUT DISTRIBUTION IN PEACH BOTTOM

Although Peach Bottom was designed for a "helium coolant inventory" of 4225 Ci of radioactivity including numerous condensable species (Ref. 9), no mention is made of plateout activity in the primary circuit - much less the distribution of that plateout. However, since the design of Peach Bottom, the amount and distribution of plateout activity have become significant design parameters because of their influence on reactor design, maintenance, and accident analysis, Therefore, methods have been developed to predict such fission product transport, namely, the PAD code. Application of such methods to Peach Bottom, and subsequent comparison of predicted and observed behavior, is useful in establishing the validity of the methodology.

The PAD code is described in detail in Ref. 2, and its essential features are reviewed in Appendix A. Briefly, PAD is a transient, one-dimensional mass transfer code; an explicit finite difference solution is obtained for the coupled, nonlinear differential equation describing the conservation of mass with a convective boundary condition. The coolant and surface concentrations are coupled by an equilibrium adsorption process; either Langmuir or Freundlich (concentration-dependent) isotherms may be employed to describe the sorption process. The model allows for production by precursor decay and treats recirculation in a closed loop. The code has three options for treating deposition: (1) no sorption (e.g., a nonadsorbing noble gas); (2) no desorption (the surface is a perfect sink or, more precisely, the vapor pressure over the surface is zero for all surface concentrations); and (3) desorption (an adsorption isotherm is employed such that at a given surface temperature and partial pressure, an equilibrium surface concentration exists beyond which no further accumulation occurs). The methods for applying PAD for LHTGR design have been documented previously (Ref. 13).

Several attempts to verify the code by analysis of experimental plateout distributions have already been made with mixed results (Ref. 14). These validation exercises included prediction of the Cs-137 distribution in Peach Bottom after Core 1 operation and comparison with ORNL gamma scans taken after 384 EFPD of Core 2 operation (the assumption was made that early Core 2 operation did not substantially alter the distribution). The predictions

appeared to be consistent with the ORNL results; however, since the measurements were concentrated in the cold ducting, the agreement could have been fortuitous.

A major problem in predicting plateout distributions is choice of appropriate sorption isotherms to describe the sorptivity of plateout surfaces for volatile fission products such as iodine and cesium. This problem, and its impact on reactor design, has been described previously (Ref. 15). The difficulty is illustrated in Appendix B for cesium plateout predictions - cesium being the dominant nuclide in the Peach Bottom primary circuit.

2. EXPERIMENTAL METHODS

The data acquisition and reduction methods employed by IRT to scan the circuit are developed in detail in the test procedures (Refs. 5,6) and are summarized in the data compilation report (Ref. 7). The material in this section was excerpted from these documents for easy reference.

2.1 EXTERNAL DUCT SCANS

The external scans were made with a Canberra Model 7229 lithium-drifted germanium detector. As an example of detector performance, it exhibited a counting efficiency of 0.08%, a resolution of 79 keV (FWHM), and a peak-to-Compton ratio of 36:1 for the 662-keV gamma ray from Cs-137. The detector was housed in a lead shield with interchangeable collimator inserts. At each duct location to be measured, the detector/collimator assembly was placed against the insulation on the side of the duct as shown in Fig. 4.

A block diagram of the electronics used to acquire and store the spectral data is shown in Fig. 5. The pulse output from the gamma ray interaction with the detector was conditioned, shaped, amplified, and then processed by a 4096 channel multichannel analyzer. After a significant number of counts had been accumulated in the analyzer, the spectral data, along with the counting time and identification information, were stored on magnetic tape. The detector signal was also transmitted to a single-channel analyzer and then to a scaler set to monitor the Cs-137 activity. The scaler data were printed out on a teletype and recorded in a log book as a backup to the tape data.

The first step in the data reduction was calculation of the peak integrals with the IRT computer code SHERRY. The next step was to relate the peak integral, hence count rate, to specific plateout activity. The

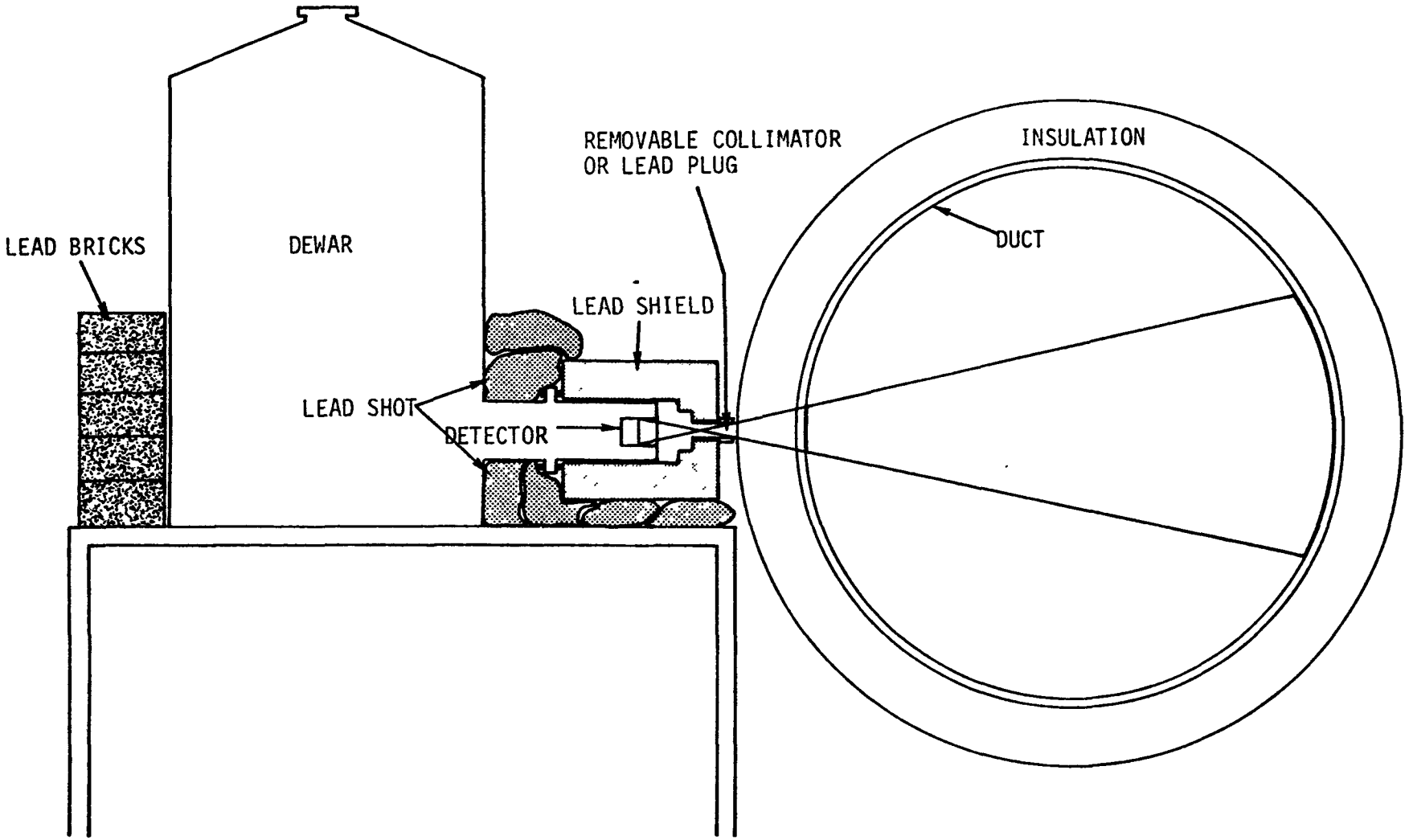

Fig. 4. Position of detector relative to standard helium duct

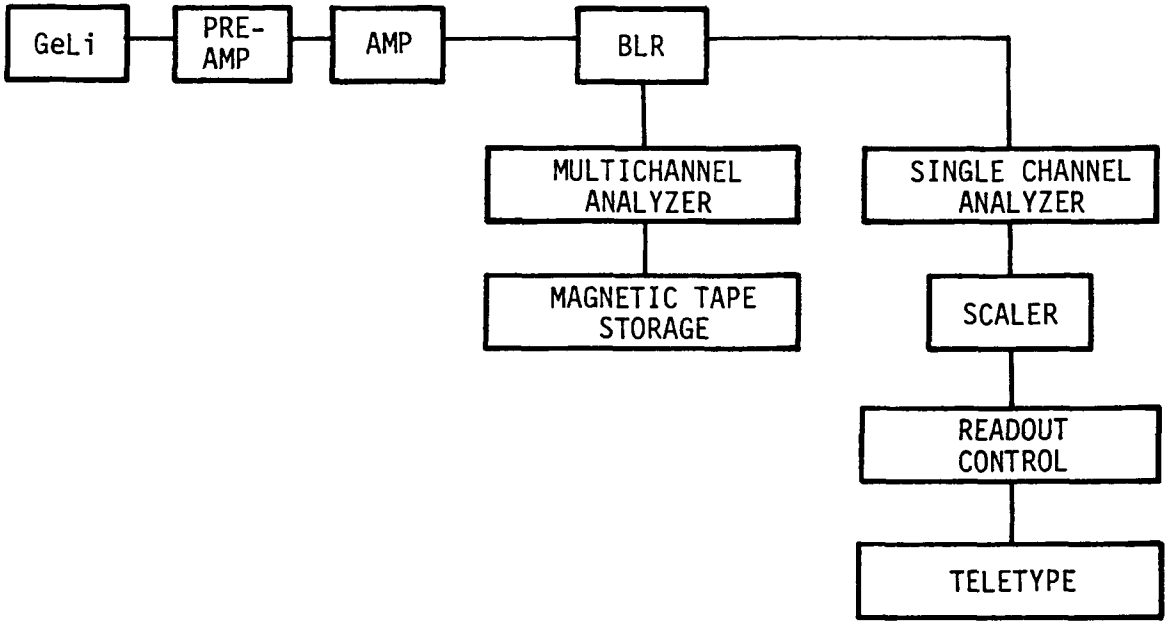

Fig. 5. Signal conditioning and data storage system

necessary collimated detector efficiency curves were generated by laboratory measurements using standard sources and mockups of the ducting and insulation. With these calibration curves, and the assumption that the plateout was locally uniform, point kernel integrations were performed over the areas seen by the detector on the near and far faces of the duct, thus giving the specific activity on the duct. A similar approach was used for the concentric duct scans, but an additional assumption had to be made regarding the relative distribution of activity between the inner and outer ducts. For calculational purposes, it was assumed (somewhat arbitrarily) that the specific activity on the inner duct was twice that on the outer duct. Recent radiochemical analysis of trepan samples taken from the inner and outer ducts tends to confirm this assumption.

2.2 STEAM GENERATOR TUBE SCANS

With the vertical U-tube design of the Peach Bottom steam generators (Fig. 2), it was apparent that the plateout distribution on the tube bundle might be mapped by lowering a detector down the inside (water side) of the tube if a suitable detector could be devised. A variety of detector types was considered; most were ruled out immediately because of the degree of miniaturization required. Laboratory tests indicated that a cadmium telluride detector could be made sufficiently small and still give resolvable spectra for Cs-134 and Cs-137 (known to be the dominant gamma emitters from the ORNL duct scans). The first attempt to obtain actual steam generator data with the CdTe detector failed because of unacceptably poor resolution. Consequently, a number of changes were made in the detector; the details are given in Ref. 7. Basically, a tantalum shield was fabricated to reduce the low-energy gamma background, the preamplifier was modified to give a faster rise time on the output pulse, and the fast-pulse analysis scheme was modified; with these changes the peaks became resolvable. However, the diameter of the shielded detector was too large to fit into the economizer tubes, and the unshielded detector did not give resolvable spectra. Therefore, for the economizer section, the scanning was accomplished with a miniature Geiger-Müller (GM) tube detector which was cross-calibrated with the CdTe detector.

A CdTe detector transporter was devised to position the detector within the steam generator tube; the apparatus is shown schematically in Fig. 6. After blowing out the tube with nitrogen, the detector/pre-amplifier assembly, affixed to the end of a coaxial (power/signal) cable, was lowered manually to the bottom of a selected tube. The exact depth was indicated by a distance scale marked on the cable. The cable was then inserted into a motor-driven, cam-controlled, take-up pulley. Sliding adjustments on the support members facilitated alignment of the take-up pulley above the tube being scanned. The scanning sequence consisted of a stationary count followed by remote activation of the drive motor, withdrawing the cable until the cam interrupted the advance after 0.15 m of travel whereupon another stationary count was taken. This sequence was repeated until the entire tube was scanned; occasionally scans were only taken at every other stop (0.3-m increments). The GM tube scans were accomplished with the same transporter.

The electronic circuitry and data storage system used for the CdTe detector measurements were generally similar to that used for the Ge(Li) scans. However, the high background of low-energy gammas in the tube bundle necessitated the use of additional signal processing techniques for the CdTe scans to provide time-of-rise selection and pulse pile-up rejection. For the GM tube measurements, the pulses were amplified, shaped by a single-channel analyzer, and accumulated in a scaler; the data were recorded manually.

Extensive calibration measurements were required to reduce the CdTe spectral data to specific plateout activity. A tube array mockup was constructed of each of the three tube bundles. Rather than coating all the tubes with radioactive cesium, 2 x 2 cm foil sources were wrapped around a tube providing a known band of activity. By systematically varying the spatial relationship between the source band and the detector within an array of tubes, spatially dependent detector response curves could be generated. As shown in Fig. 7, the tubes surrounding the tube containing the detector (tube 1) could be grouped into a number of classes, each characterized by a detector response curve as illustrated

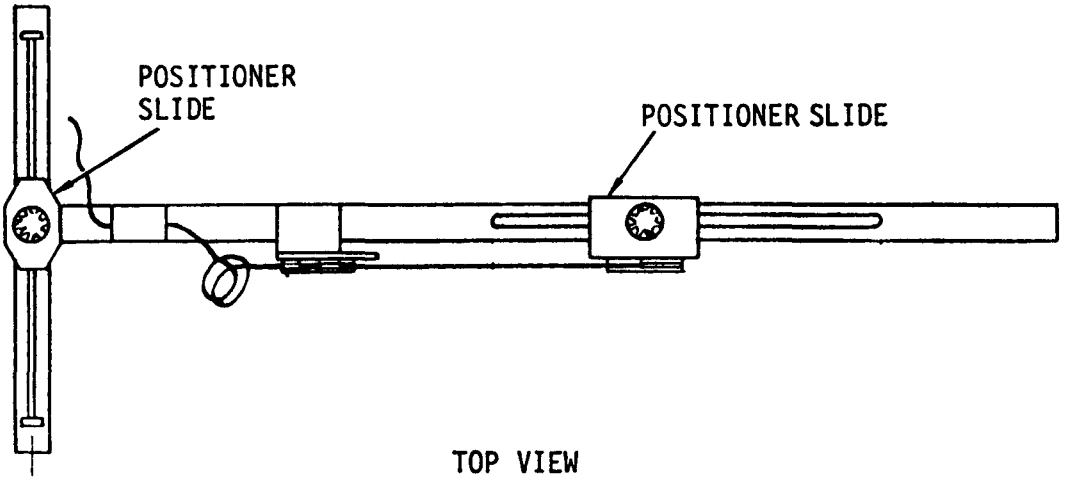

TOP VIEW

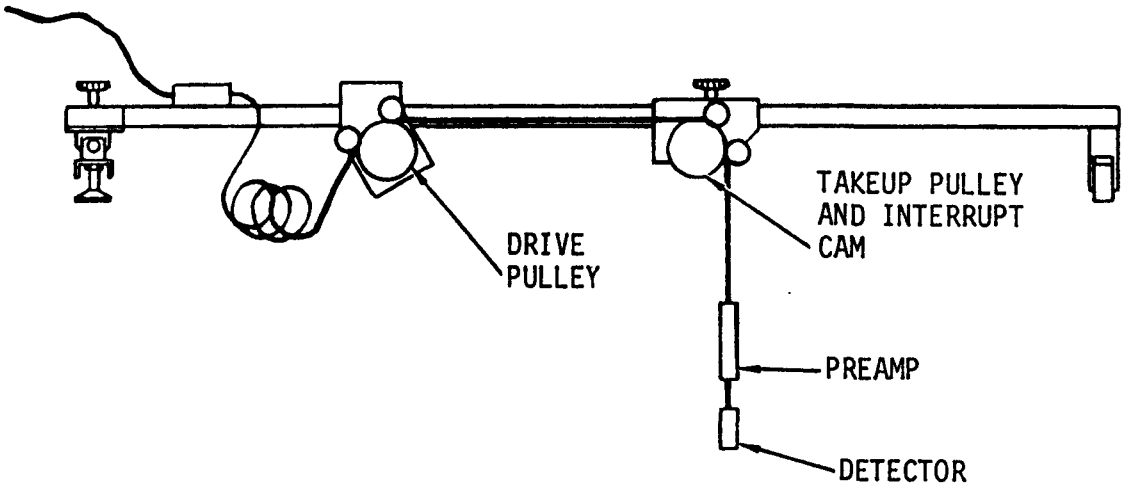

SIDE VIEW

Fig. 6. CdTe detector positioning apparatus

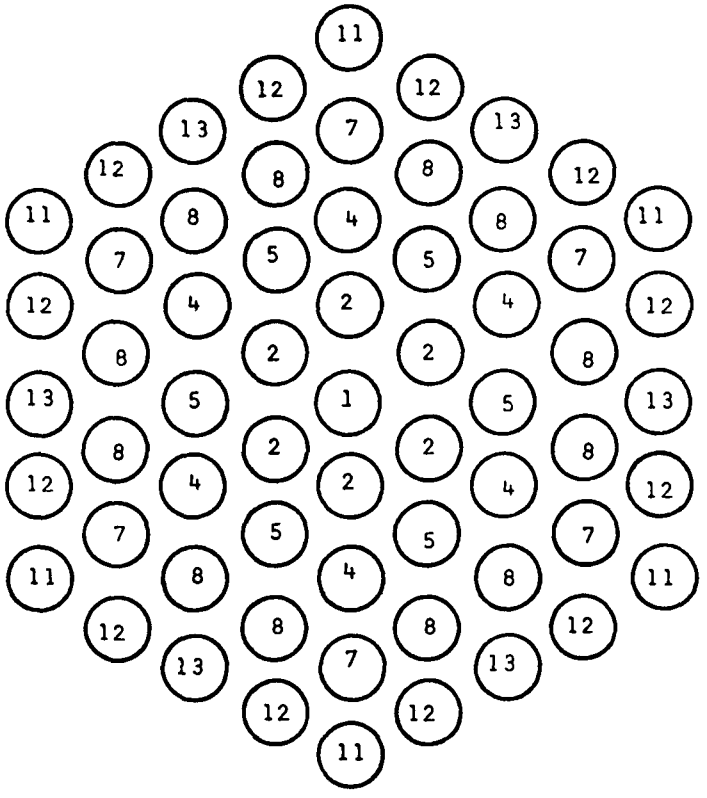

Fig. 7. Location of each class of steam generator tube relative to tube being measured (tube 1)

in Fig. 8. Finally, assuming that the specific activity was locally uniform, the total detector response for a given specific activity could be determined by integration. To reduce the data from a particular tube scan, it was necessary to determine the number of tubes of each class which influence the detector response and to sum these to obtain the total response. This calibration scheme did not account for large nonlinear gradients or the presence of support baffles or the tube bundle shroud; hence, some data reduction errors must be expected. Since the GM tube gave no spectral resolution, it was impossible to determine the individual isotopic contributions from the GM data alone. However, since the Cs-137/Cs-134 ratio was apparently constant in the evaporator section and the cold ducting, it was assumed that the ratio was also constant in the economizer. Therefore, a cross-calibration between the CdTe detector and the GM tube was developed by taking identical sets of measurements in evaporator outlet tube 102. The effect of geometry differences between the economizer and evaporator sections was accounted for by measurements on an economizer array mockup.

Cesium-134 has two prominent gamma rays at 0.605 and 0.796 MeV; Cs-137 has a single gamma ray at 0.662 MeV. As illustrated in Figs. 9 and 10, the 0.605-MeV peak of Cs-134 and the 0.662-MeV peak of Cs-137 are not completely resolved, substantially complicating data reduction. The solution adopted is detailed in Ref. 7. Basically, the Cs-134 response is determined by integrating the 0.796-MeV peak, which is completely resolved. Then the composite signal from the 0.605 and 0.662 peaks is determined. Since the Cs-134 contribution can be inferred from the 0.796-MeV response, the Cs-137 response is obtained by difference. Obviously, this numerical "stripping" technique introduces additional uncertainty into the Cs-137 results.

2.3 INTERNAL DUCT SCANS

The internal duct scans were performed with an intrinsic (non-lithium drifted) germanium detector built by Applied Detector Corporation. The advantage of such a detector compared to a standard Ge(Li) detector is that it needs liquid nitrogen only when being operated. Thus, its cryostat can be made quite small, resulting in a relatively compact, lightweight unit

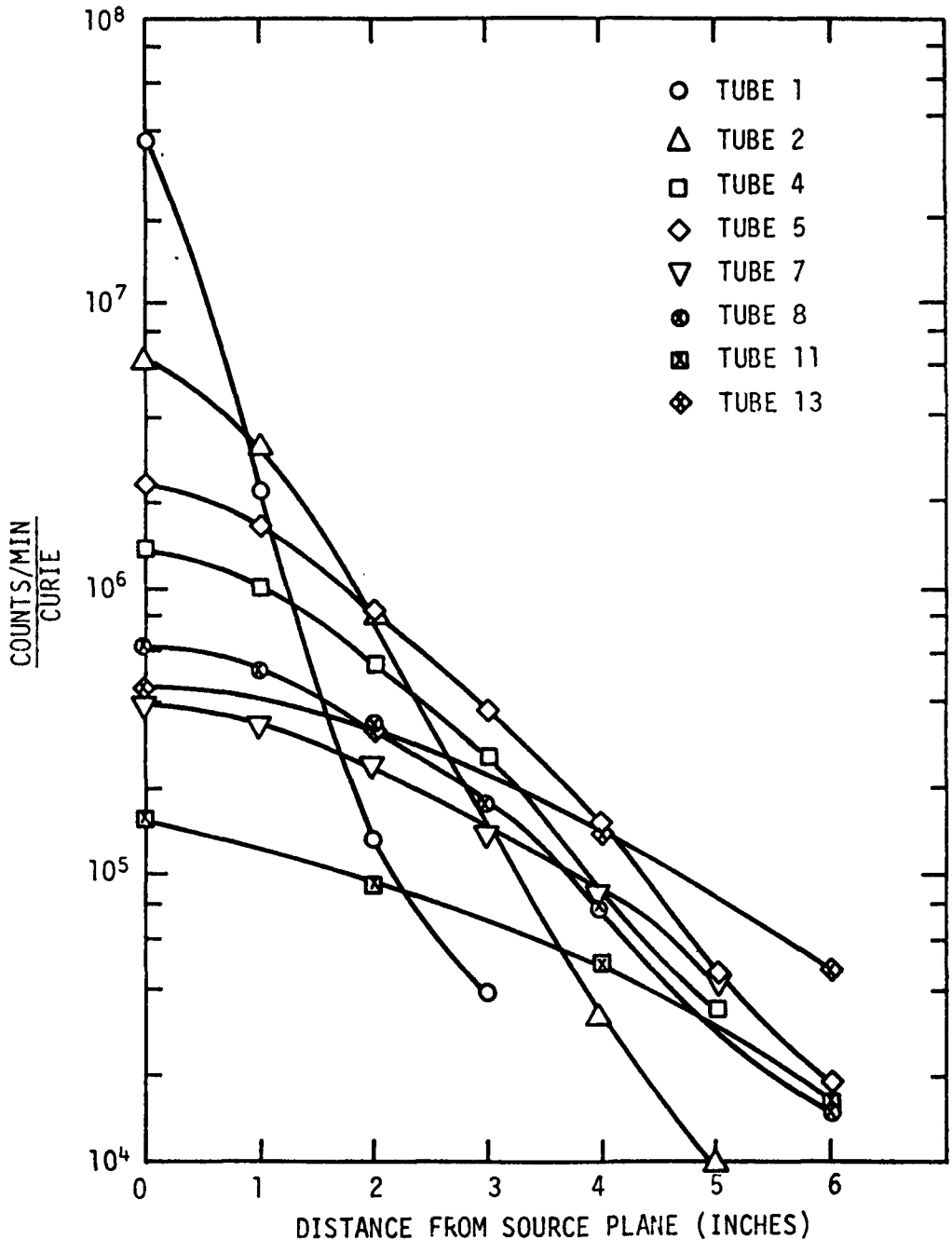

Fig. 8. CdTe detector calibration for 0.796-MeV gamma ray of Cs-134 in superheater tubes

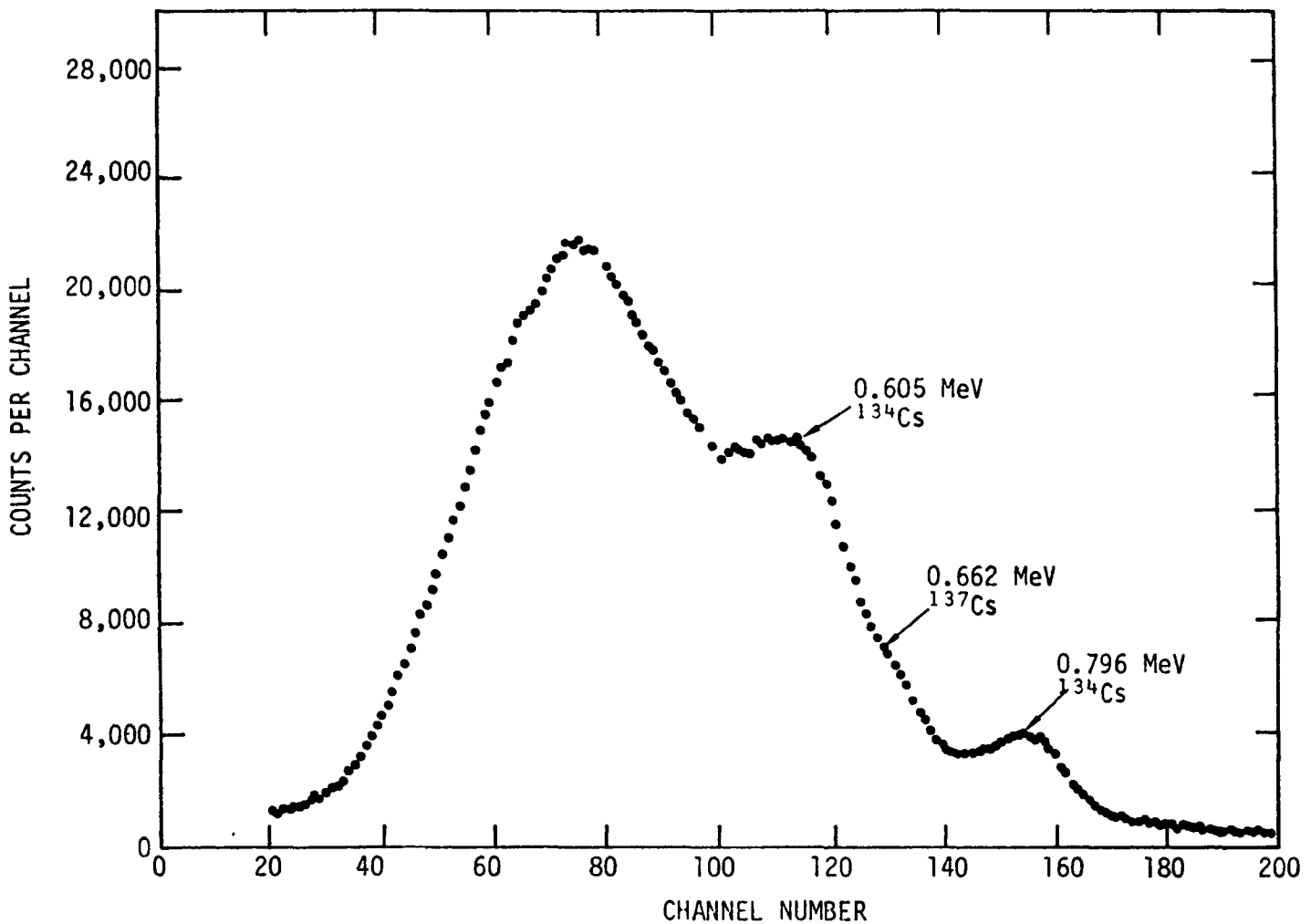

Fig. 9. Typical spectrum of a steam generator tube taken with a shielded CdTe detector

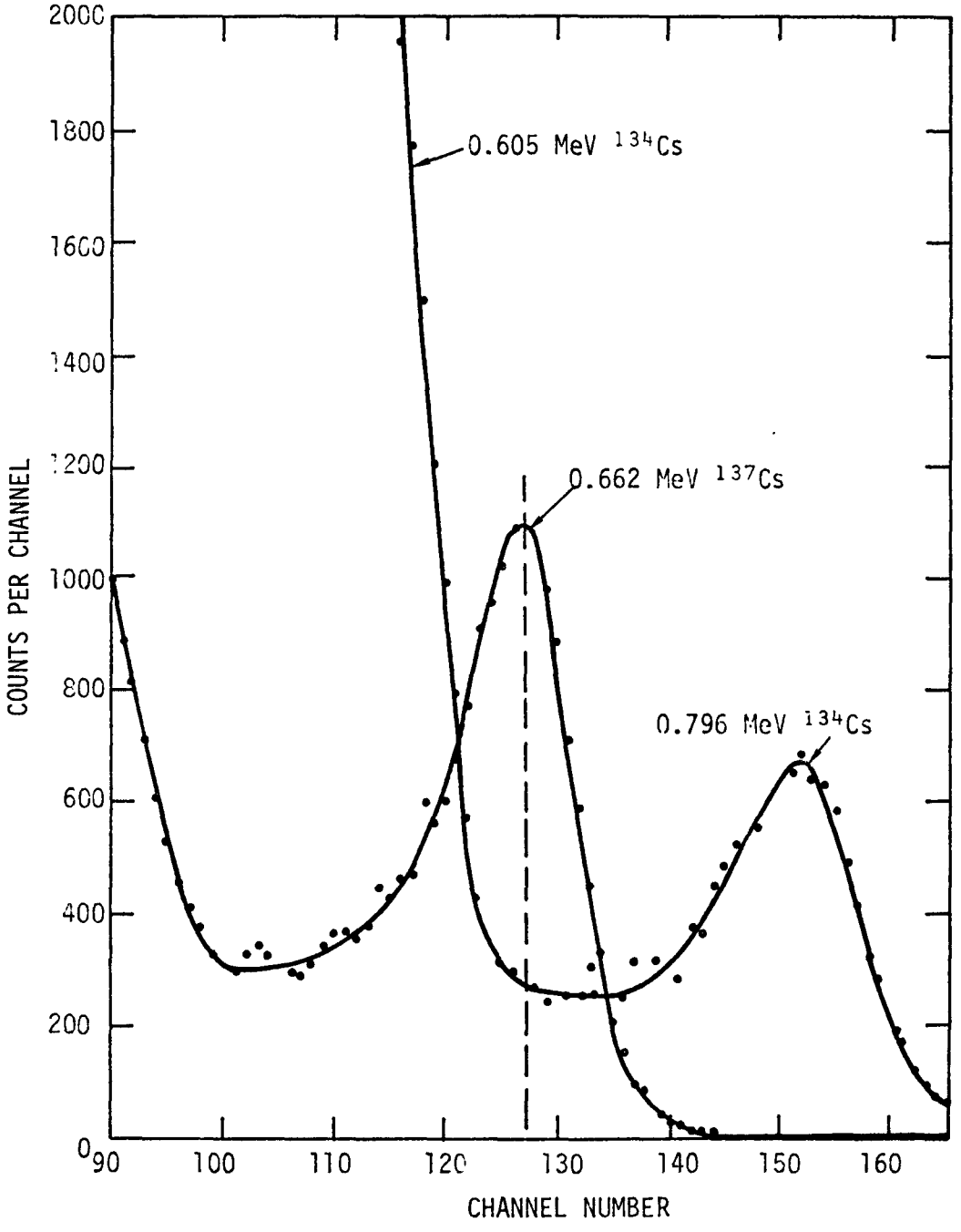

Fig. 10. Superimposed spectra of Cs-134 and Cs-137 taken with a shielded CdTe detector

suitable for use as a travelling detector. The detector/cryostat assembly was placed in a carriage designed to maintain the centerline of the detector effectively coincident with the centerline of the duct. In addition, the detector was equipped with a lead collimator which limited the "viewing angle" of the detector to approximately a 0.32-m band around the inside surface of the duct. The detector transport mechanism, electronic circuitry and data storage hardware were conceptually similar to that used for the steam generator scans.

Calibration of the internal scan measurements was quite straightforward because of the symmetrical geometry and the absence of absorbing media between the detector and the plateout activity. Known sources were placed on a line parallel to the detector centerline and displaced from it a distance equal to the inner radius of the duct. The detector response was then recorded as a function of displacement from the midplane of the detector sensitive volume. To apply this calibration to the reduction of actual spectral data, it again had to be assumed that the plateout activity was locally uniform, the only complication was the effect of plateout on adjacent ducts. (The two vertical ducts scanned were in a cavity containing four parallel ducts centered on the corners of an imaginary 1.5-m square.) A computer routine was written to perform a point kernel calculation of the contributions of activity on adjacent ducts to the total detector response. Assuming uniform activity on all ducts, the duct containing the detector was shown to produce >90% of the detector response.

3. RESULTS

3.1 EXPERIMENTAL RESULTS

3.1.1 External Gamma Scans

The specific activities of gamma-emitting radionuclides were determined by external Ge(Li) scans at the 12 locations shown approximately in Fig. 1. Since these locations were chosen to complement the ORNL scans which were all in loop 1, the IRT scans were concentrated in loop 2; however, three common points in loop 1 were measured to assure cross-calibration between the ORNL and the IRT scans. These gamma-scan locations are defined more precisely in Figs. 11 through 15 as are the locations where trepan samples were removed. (ORNL scan locations are identified as ORNL-Y, IRT scan locations as IRT-X-Y, and GA trepan sample locations as TS-Y, where X is the loop number (1 or 2) and Y is the location number.) The IRT measurements were made in May 1975, some 7 months after final reactor shutdown; thus, any short-lived radionuclides would have already decayed. However, the ORNL measurements were made within a week of final shutdown.

The dominant gamma emitters identified in the spectra were Cs-134 and Cs-137. Occasionally, Co-60 was indicated in the ORNL results, but IRT only found one of two characteristic Co-60 peaks. ORNL found no I-131 at EOL, even though the isotope had been identified during the 818 EFPD shutdown scan (Ref. 12). Apparently, the I-131 signal was lost in the cesium background. The reduced IRT data, decayed back to final shutdown on October 31, 1974, are tabulated in Table 1. The concentric duct data are still somewhat tentative. In general, the specific activity decreased in the direction of coolant flow.

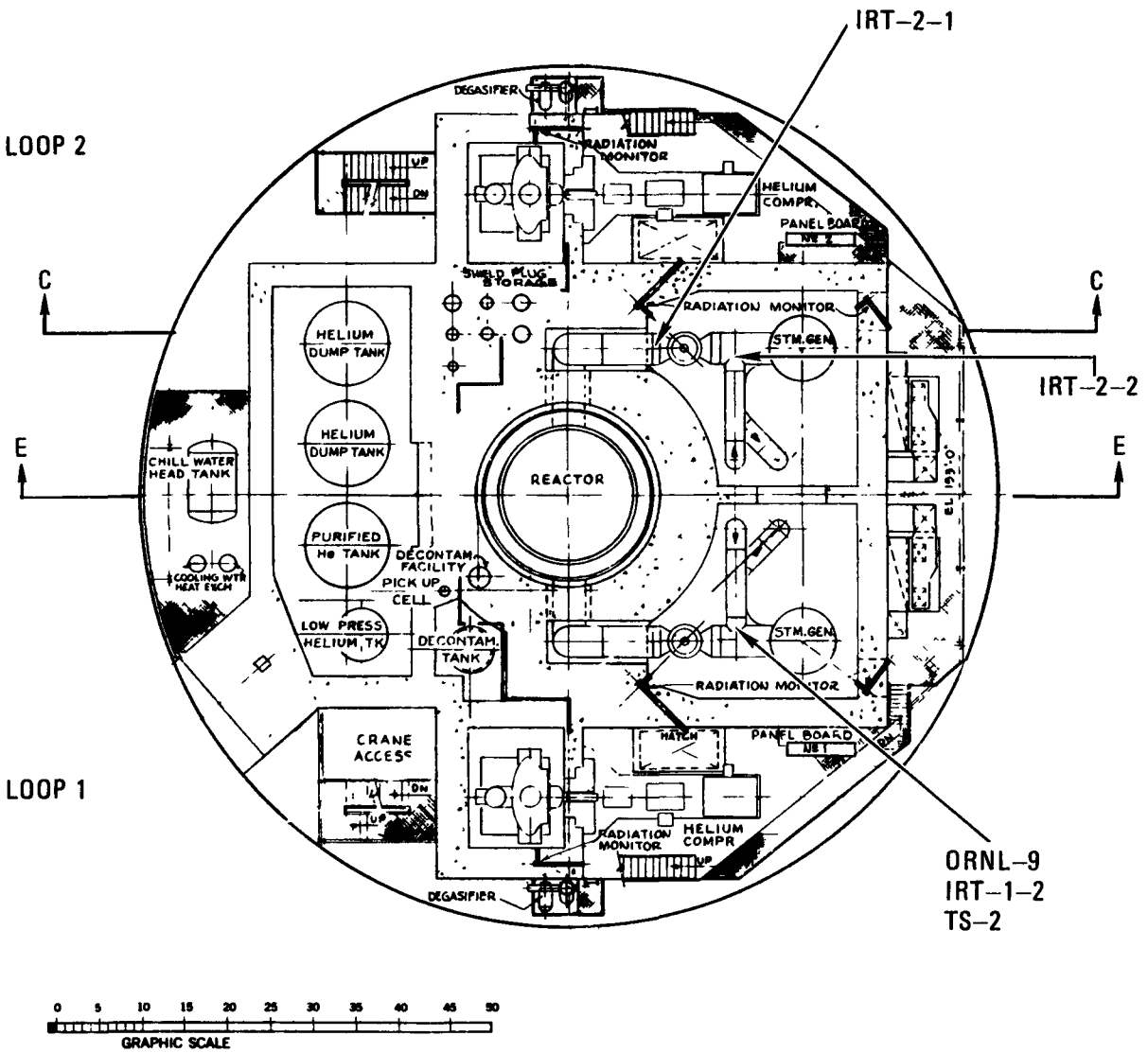

Fig. 11. Plan view A-A showing positions 1 and 2

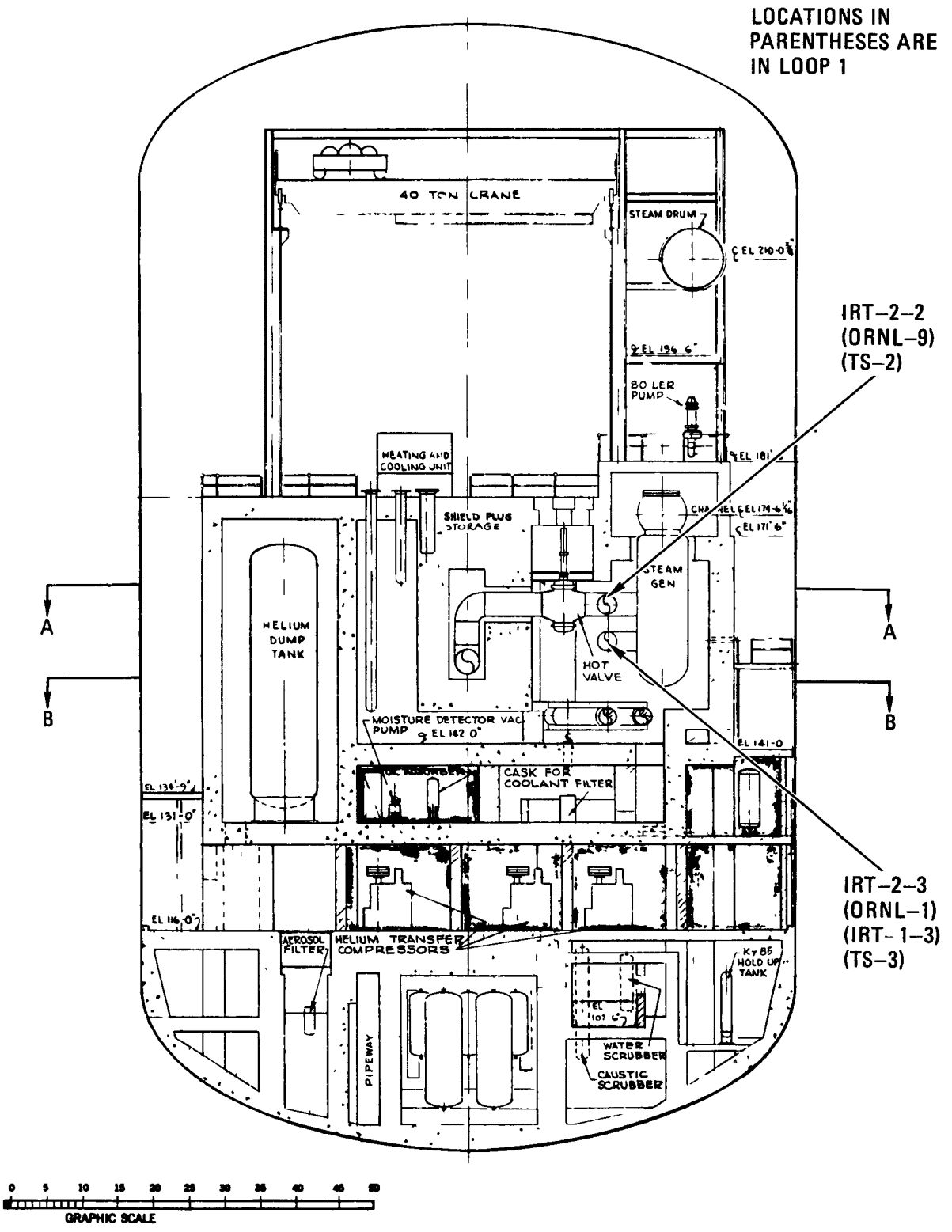

Fig. 12. Elevation view C-C showing position 3

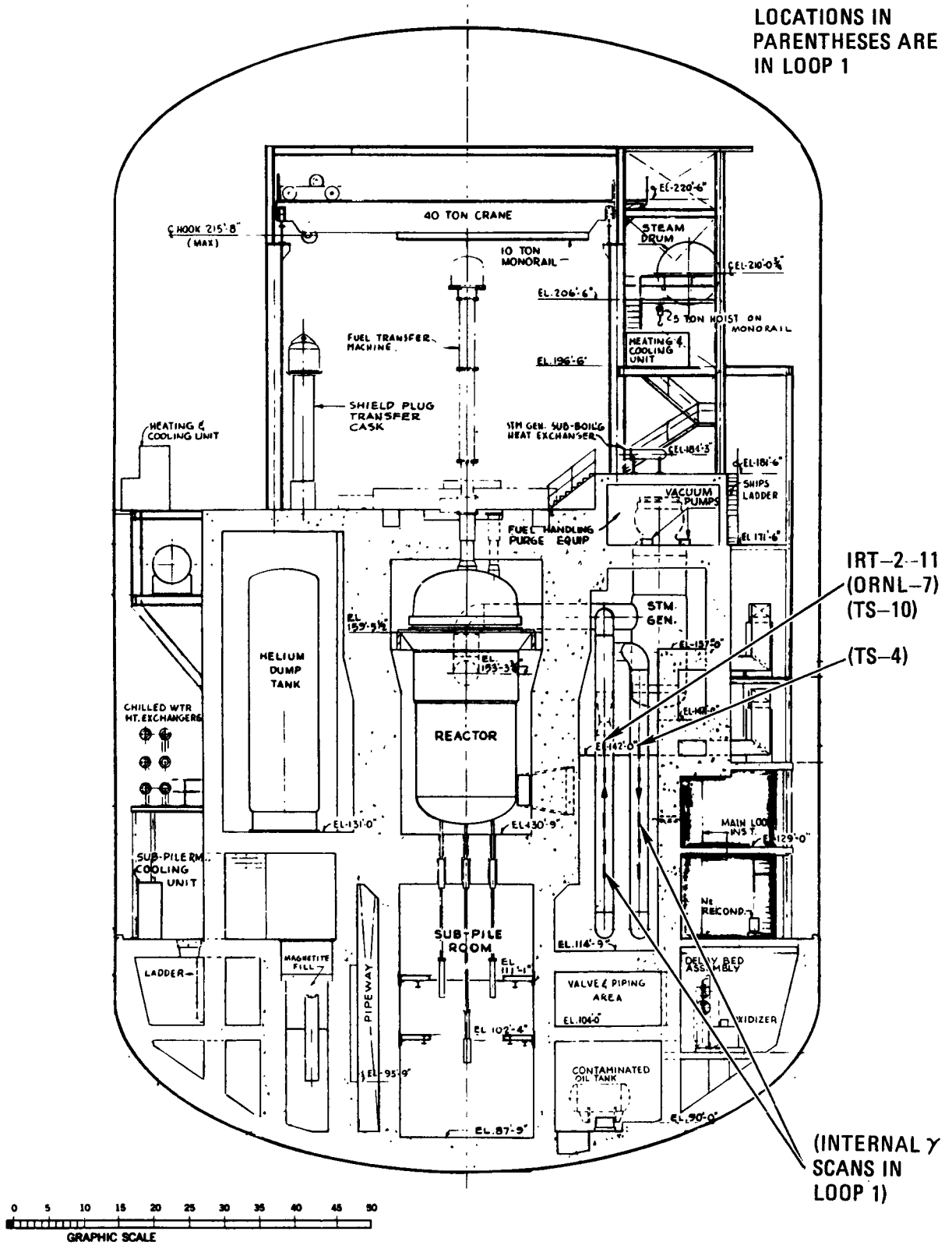

Fig. 13. Elevation view E-E showing positions 4 and 10 (both 4 and 10 are at elevation 144 ft 0 in.)

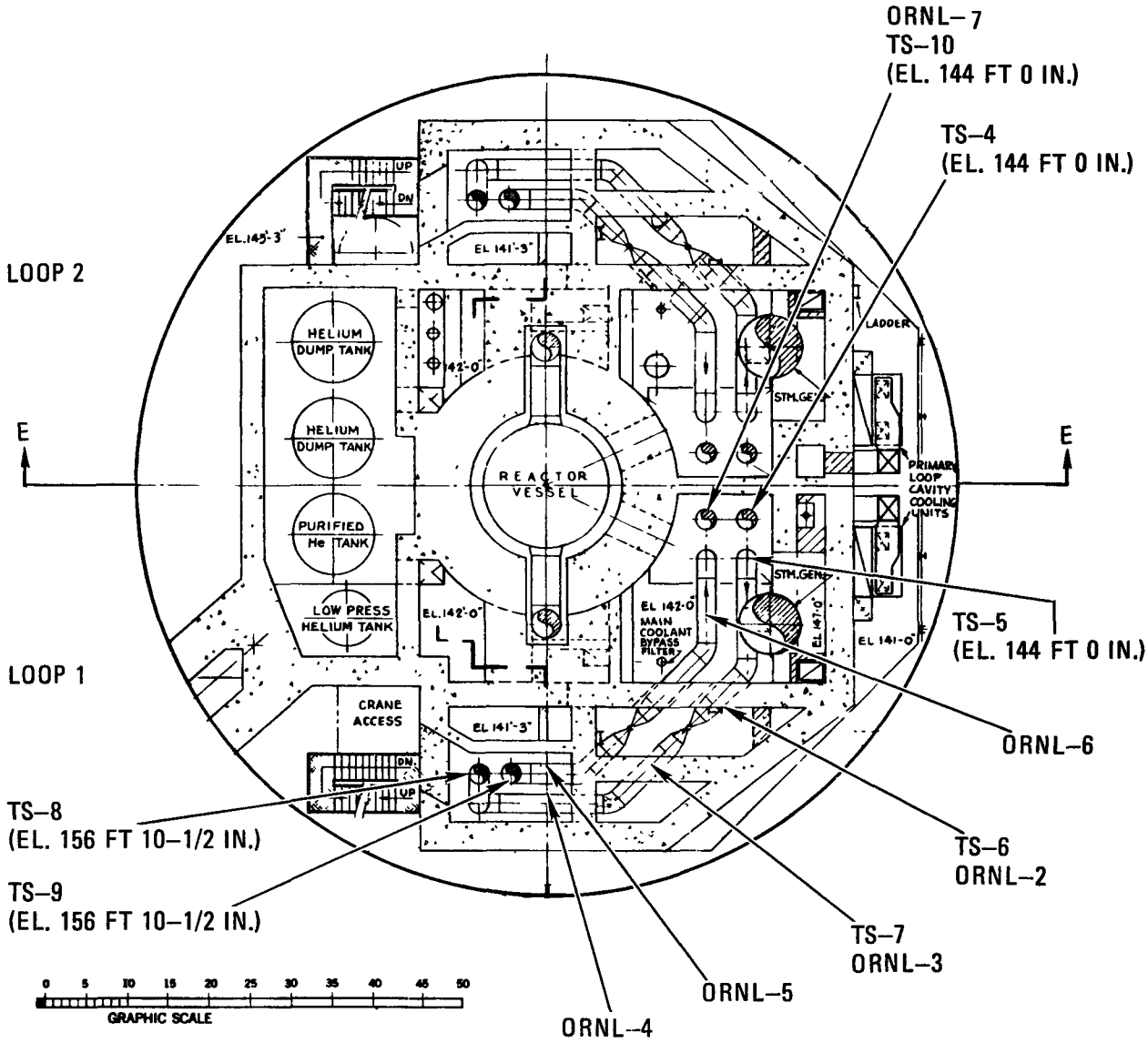

Fig. 14. Plan view B-B showing positions 4 through 10 (4, 5, and 10 are at elevation 144 ft 0 in. - 2 in. above floor at 142 ft 0 in.)

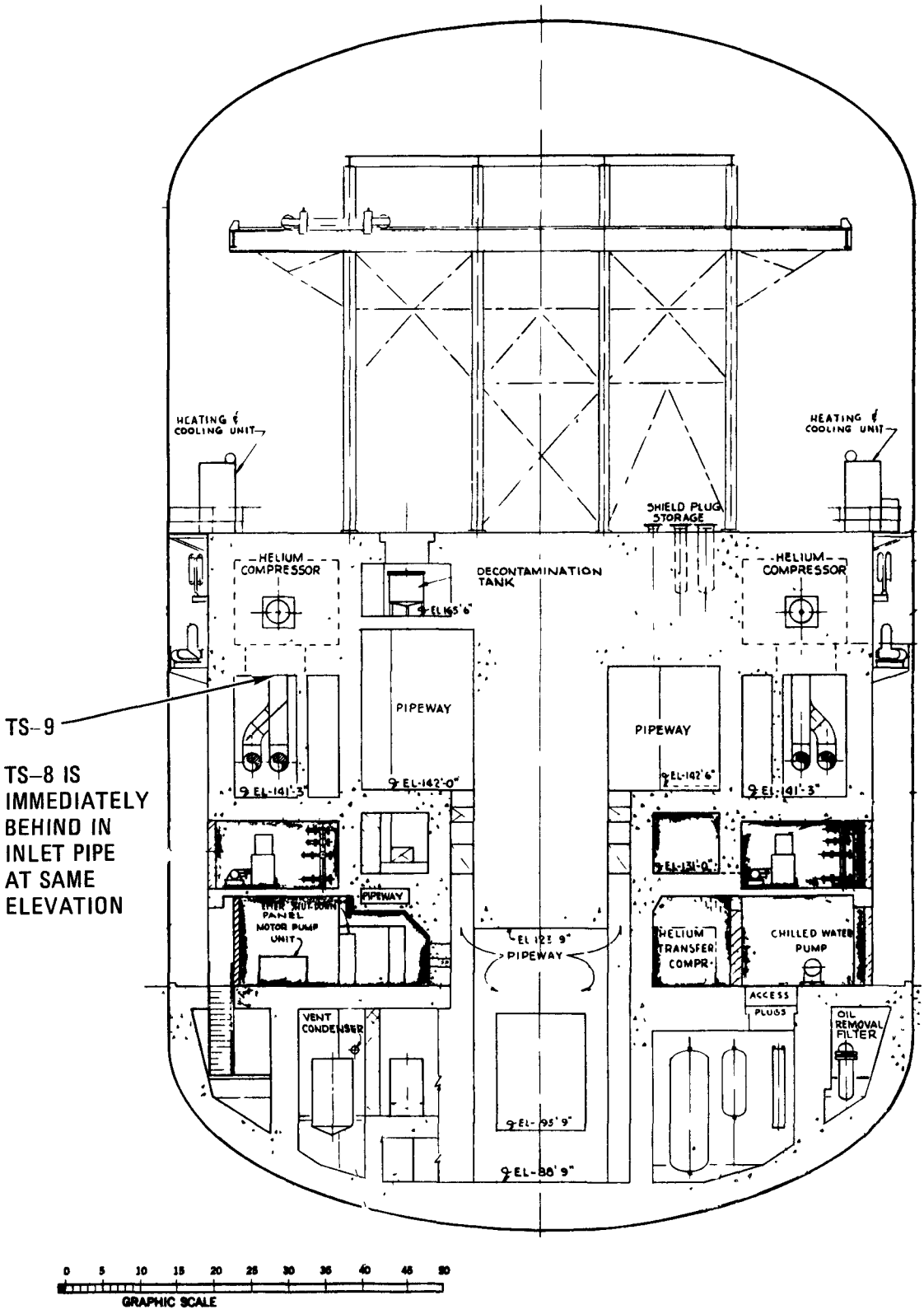

Fig. 15. Elevation view D-D showing positions 8 and 9

TABLE 1

HELIUM DUCT CESIUM PLATEOUT INTENSITIES AS MEASURED EXTERNALLY[a,b]

Position	Cs-137 (μCi/cm^2)	Cs-134 (μCi/cm^2)	Ratio (Cs-137/Cs-134)
Loop 2			
2-1 (inner)	2.08	2.16	0.96
2-2 (inner)	1.50	1.90	0.79
2-3	2.65	3.07	0.86
2-4	1.60	2.01	0.80
2-5	1.47	1.62	0.91
2-7	1.49	1.83	0.81
2-8	1.36	1.69	0.80
2-10	1.24	1.53	0.81
2-11	1.32	1.72	0.77
2-1 (outer)	1.04	1.08	0.96
2-2 (outer)	0.77	0.96	0.80
Loop 1			
1-2 (inner)	1.30	1.80	0.72
1-3	2.22	2.62	0.85
1-7	1.82	2.17	0.84
1-2 (outer)	0.66	0.88	0.75

(a) All activities are decayed back to final shutdown on October 31, 1974.

(b) 1 μCi = 370 Bq/mm^2.

3.1.2 Steam Generator Scans

As described in Section 2.2, the first attempts to scan the steam generator in May 1975 were unsuccessful because of detector saturation; subsequent to detector modification, those tubes shown in Fig. 3 were scanned in September 1975. Since several thousand spectra were obtained, all of which are included in the data compilation report, these data will only be highlighted herein. The essential trends in the data are illustrated in Figs. 16 through 19. Figures 16, 17, and 18 give the axial-average (along the length of the tube) Cs-137 activity for selected tubes in the superheater, evaporator, and economizer sections, respectively; Fig. 19 gives the axial Cs-137 distribution along tubes strategically located on the tube bundle axis of symmetry.

As with the duct scans, only Cs-137 and Cs-134 peaks were observed in the steam generator scans. (This observation has been confirmed by the Ge(Li) scans of the destructively removed tube samples.) Inspection of the axial-average profiles shows that the specific cesium activity decreases with depth of penetration into the tube bundle and appears to be symmetrical about the geometric axis of symmetry (e.g., consider the five tubes scanned in the leading row of the evaporator inlet). Inspection of the axial profiles in Fig. 19 reveals a significant entrance effect in the superheater inlet section. The specific activity is highest where the inlet helium jet impinged on the tube bundle and lowest at the upper and lower ends of the bundle, suggesting a maldistribution of coolant flow despite the presence of flow baffles designed to distribute the flow uniformly along the length of the bundle. This apparent entrance effect damped out with penetration into the tube bundle, giving rise to an essentially uniform profile at the exit of the economizer inlet section. The locations of the horizontal tube support baffles are also clearly indicated by periodic depressions in the axial plateout profiles; however, the magnitude of these decreases is somewhat exaggerated since the calibration scheme did not account for the energy attenuation of the support baffles.

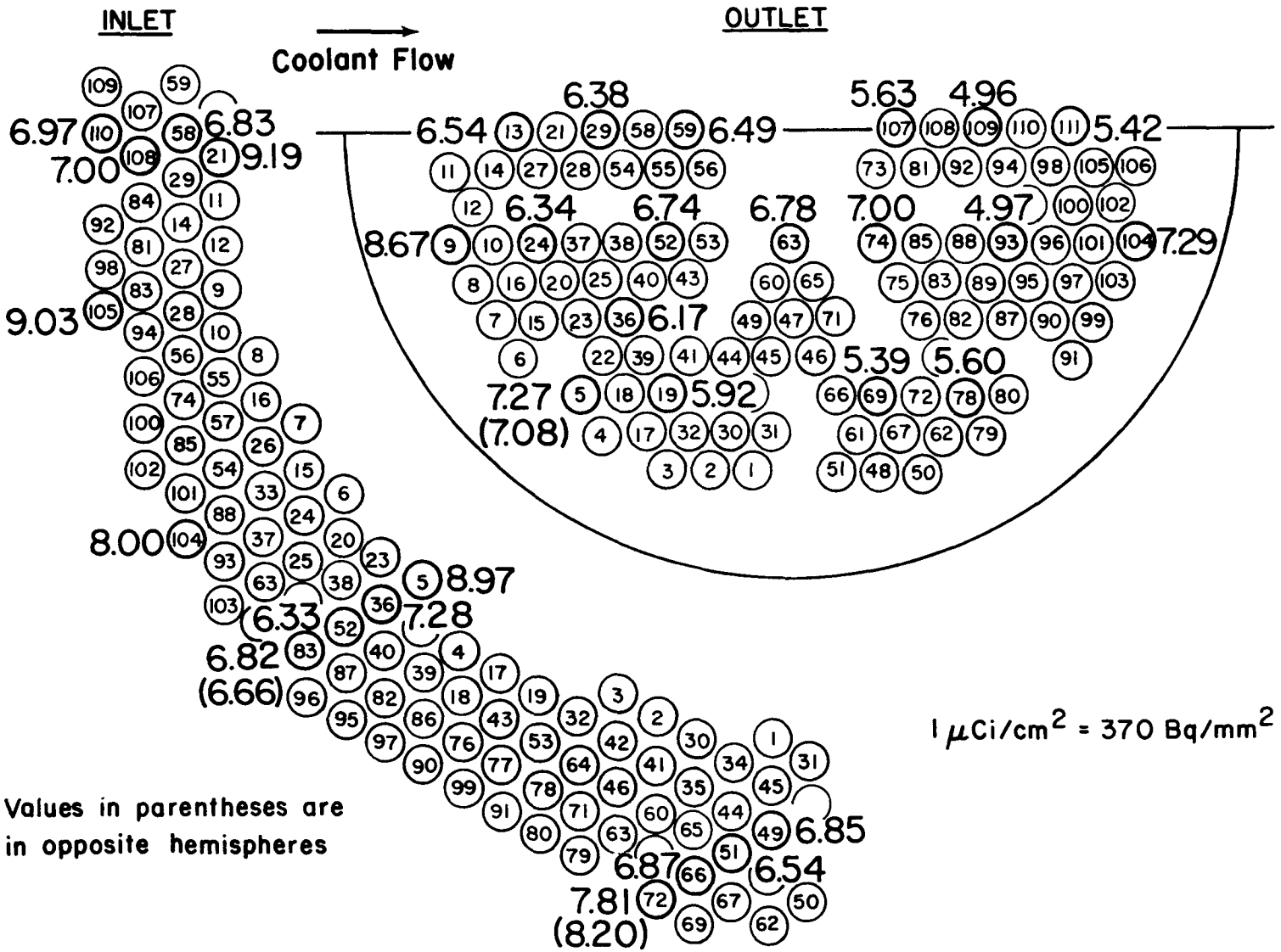

Fig. 16. Cs-137 plateout distribution in steam generator superheater, axial average specific activity ($\mu Ci/cm^2$)

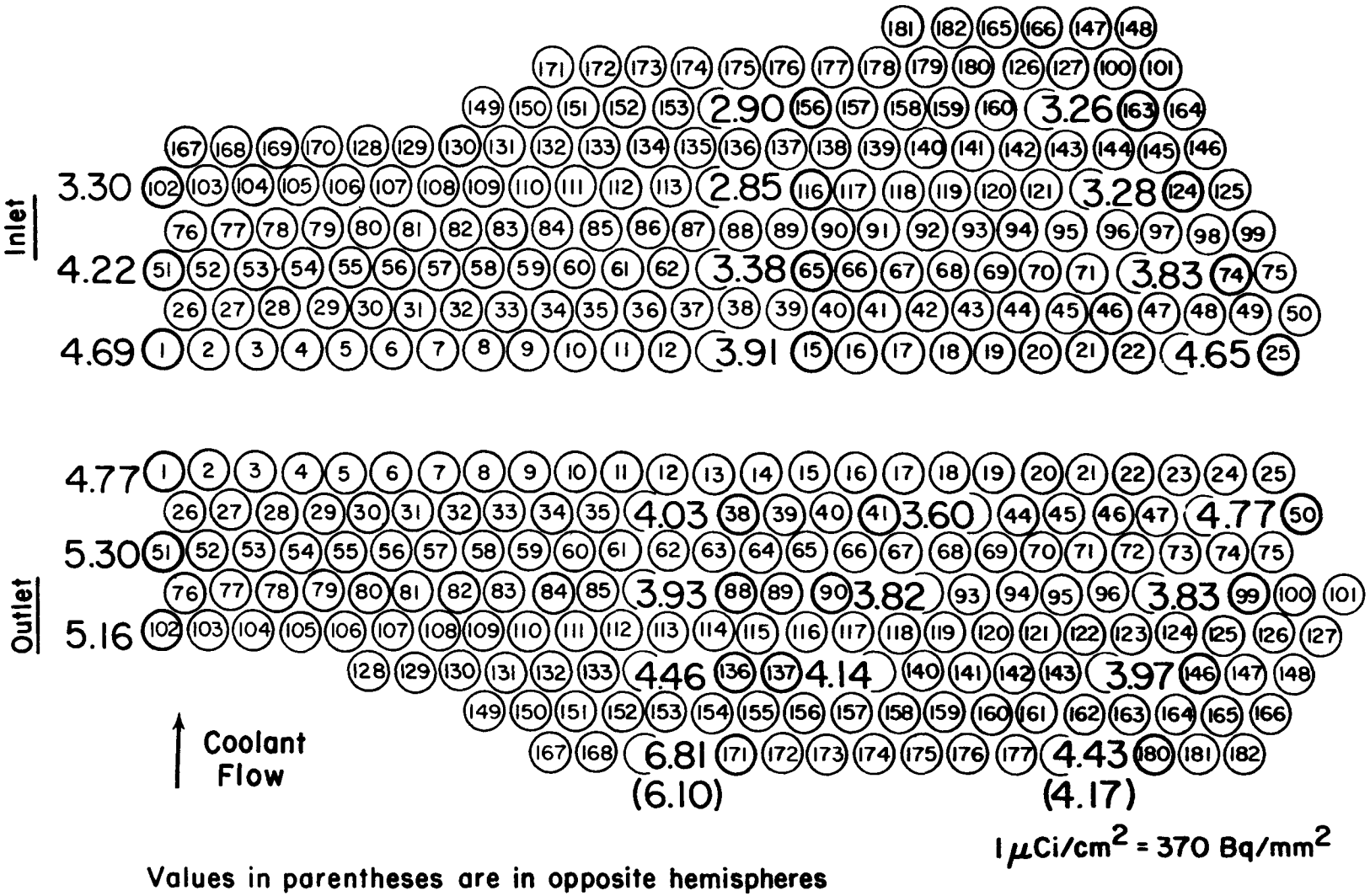

Fig. 17. Cs-137 plateout distribution in steam generator evaporator, axial average specific activity ($\mu Ci/cm^2$)

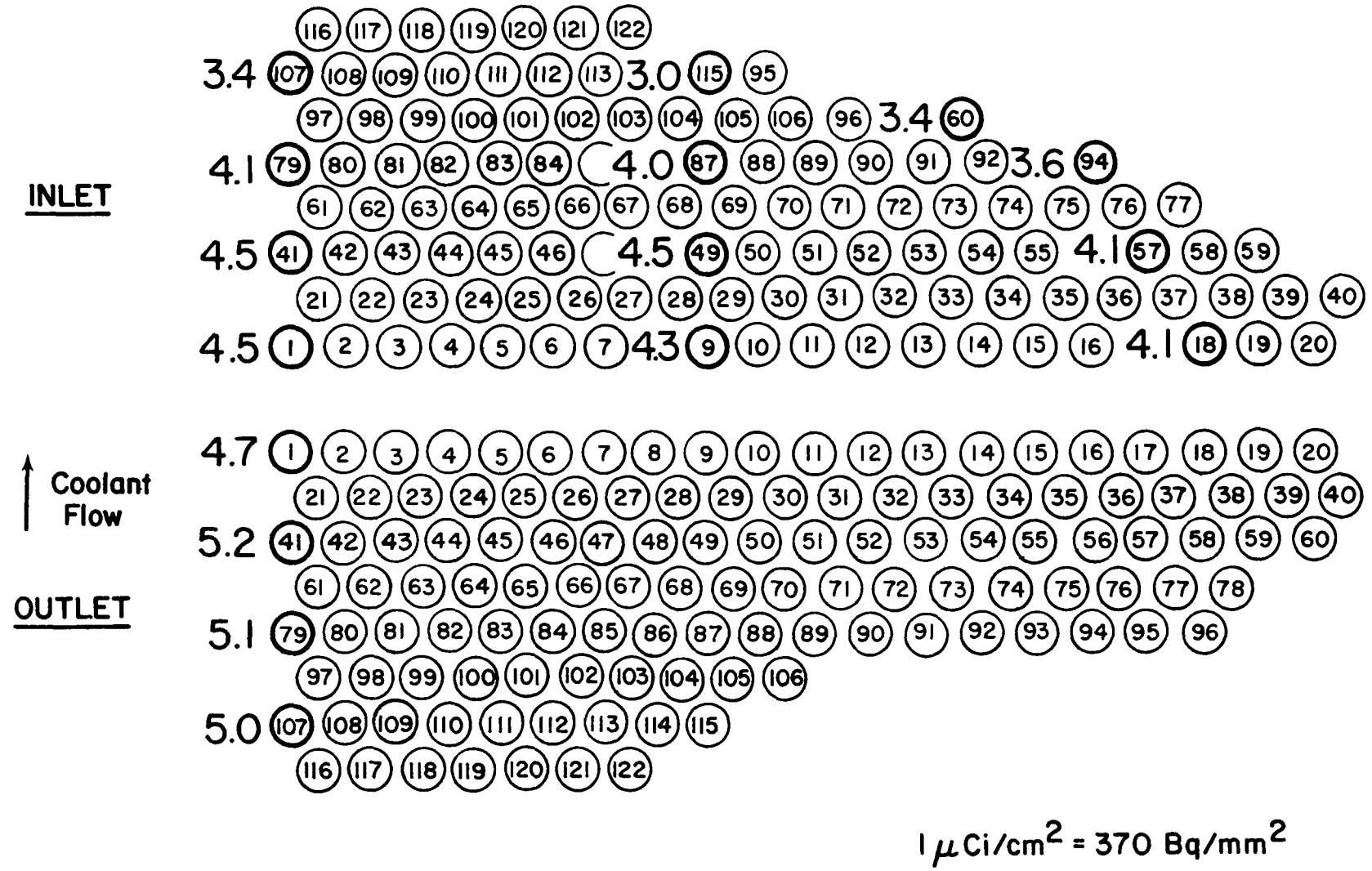

Fig. 18. Cs-137 plateout distribution in steam generator economizer, axial average specific activity ($\mu Ci/cm^2$)

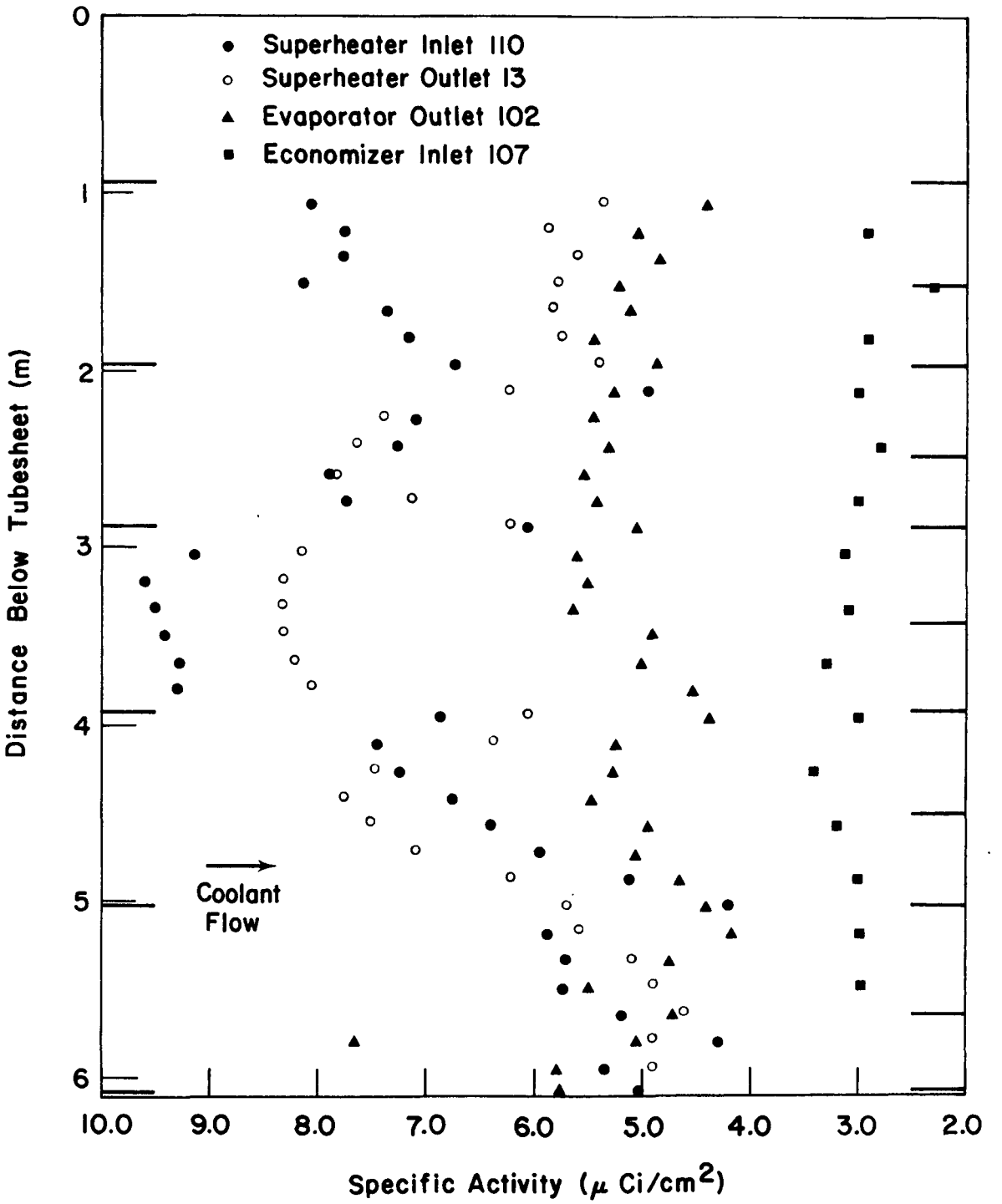

Fig. 19. Axial Cs-137 plateout distribution

3.1.3 Internal Duct Scans

Upon removal of trepan samples TS-4 and TS-10 (see Fig. 16), two 6-m-long straight runs of vertical ducting, previously inaccessible, were scanned with an intrinsic germanium detector. Spectra were obtained at 0.15 to 0.30 m increments by stationary counting; each "local" measurement is the area average specific activity in a band approximately 0.32 m high. The results are tabulated in Table 2 and displayed graphically in Fig. 20. Again only Cs-137 and Cs-134 were detected. The specific activity exhibited little local variation, with only a modest decrease in the direction of coolant flow.

3.2. DATA CORRELATION AND PAD CODE MODELING

A primary reason for gamma scanning the Peach Bottom circuit was to provide a test case for PAD code plateout predictions. Before a comparison could be made between the predicted and measured distributions, a number of problems had to be solved. These problems can be broadly grouped into PAD code modeling and data correlation categories.

The first step in applying PAD to Peach Bottom is construction of an appropriate one-dimensional model of the primary circuit. Since PAD represents exactly only turbulent flow inside circular conduits, other more complex geometries must be modeled as an equivalent number of parallel tubes characterized by an appropriate length and hydraulic diameter. Typically, the most difficult task is obtaining an accurate representation of the steam generator tube bundles; this section is of particular importance in that much of the total plateout inventory is expected to deposit in the steam generator. Craig (Ref. 16) had already prepared a PAD model of the Peach Bottom tube bundle which represented the essential features, as shown in Table 3. A slightly modified version of his model was used in this study: the superheater section was divided into two equal sections to facilitate modeling the surface temperature distribution. The other major sections of the circuit were modeled in a similar manner with the exception of the circulator; since no detailed plateout distribution was determined

TABLE 2

INTERNAL DUCT SCANS[a]
($\mu Ci/cm^2$)

Position (m)	Location 1-4		Location 1-10	
	Cs-137	Cs-134	Cs-137	Cs-134
0.0	--	--	0.85	1.17
-0.15	1.51	1.98	--	--
-0.30	1.53	1.98	0.85	1.14
-0.46	1.45	1.98	--	--
-0.61	1.48	1.93	0.85	1.11
-0.76	1.44	1.83	--	--
-0.91	1.44	1.98	0.86	1.11
-1.07	1.42	1.93	--	--
-1.22	1.43	1.90	0.81	1.03
-1.37	1.45	1.89	--	--
-1.52	1.44	1.93	0.82	1.08
-1.68	1.50	1.92	--	--
-1.83	1.50	1.98	0.82	1.09
-1.98	1.45	1.93	--	--
-2.13	1.45	1.90	0.81	1.11
-2.29	1.45	1.93	--	--
-2.44	1.44	1.95	0.80	1.08
-2.59	1.42	1.95	--	--
-2.74	1.41	1.87	0.79	1.06
-2.90	1.43	1.90	--	--
-3.05	1.39	1.86	0.78	1.09
-3.20	1.40	1.92	--	--
-3.35	1.38	1.93	0.80	1.09
-3.51	1.39	1.84	--	--
-3.66	1.41	1.92	0.80	1.08
-3.81	1.38	1.90	--	--
-3.96	--	--	0.80	1.08
-4.11	1.39	1.84	--	--
-4.27	--	--	0.82	1.11
-4.57	1.36	1.83	0.81	1.09
-4.88	1.33	1.90	0.83	1.12
-5.18	1.37	1.89	0.85	1.09
-5.49	--	--	0.85	1.17
-5.64	1.37	1.90	--	--
-5.79	--	--	0.87	1.15
-6.10	1.38	1.87	0.86	1.17

[a] 1 $\mu Ci/cm^2$ = 370 Bq/mm^2

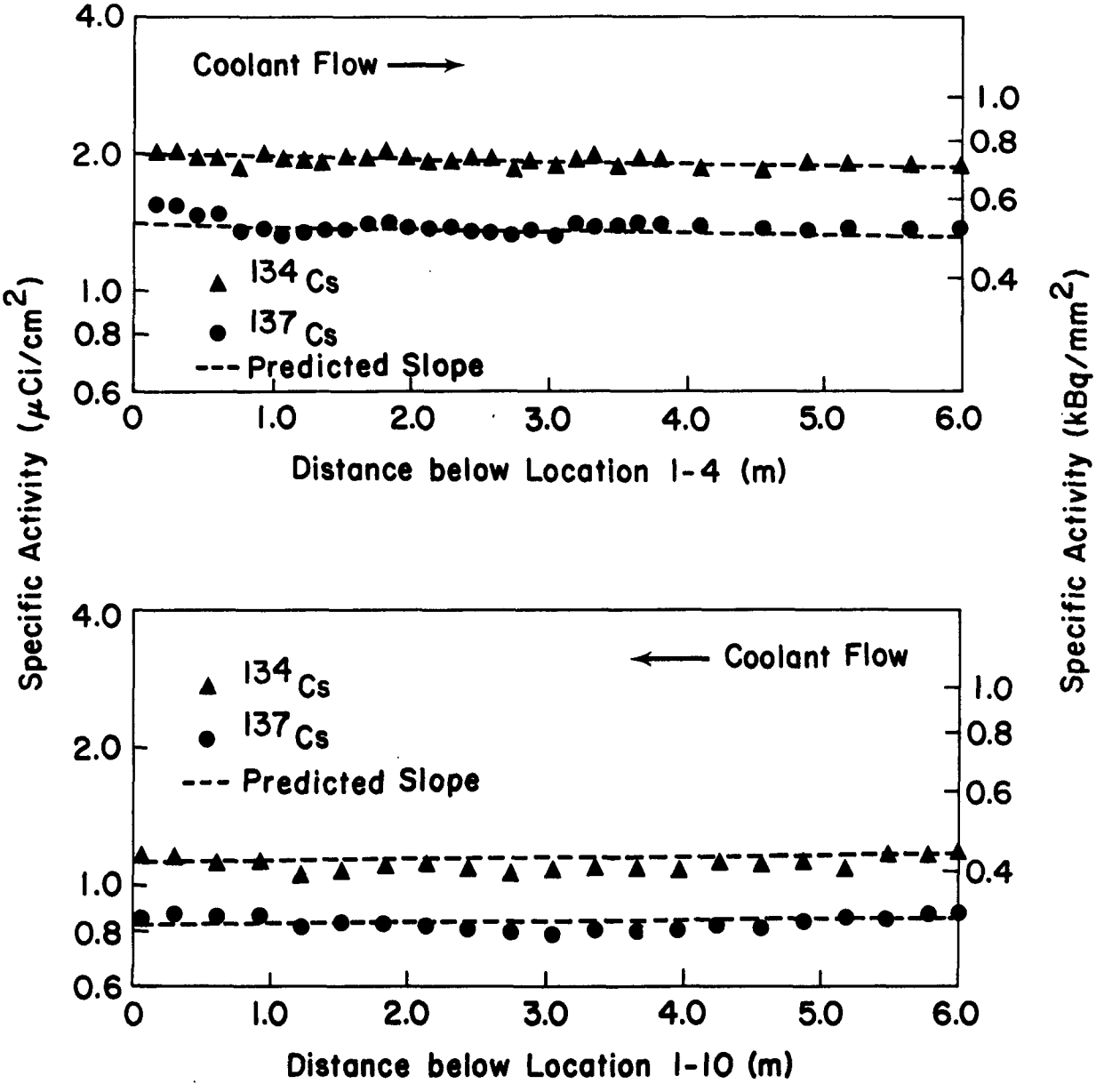

Fig. 20. Cesium profiles determined by internal duct scans

TABLE 3

PEACH BOTTOM STEAM GENERATOR[a]

	PAD Model	Actual Value
Superheater		
Surface area, cm^2	1.3×10^6	1.3×10^6
Hydraulic diameter, cm	1.905	-
Number of equivalent channels	4984	-
Length, cm	43.5	47.5
Coolant temperature at entrance, °C	693	693
Surface temperature at entrance, °C	510	510
Average velocity, cm/sec.	1680	1680
Average Reynolds No.	9665	9669
Evaporator		
Surface area, cm^2	2.25×10^6	2.25×10^6
Hydraulic diameter, cm	1.905	-
Number of equivalent channels	5560	-
Length, cm	67.6	38
Coolant temperature at entrance, °C	583	583
Surface temperature at entrance, °C	343	343
Average velocity, cm/sec	1309	1309
Average Reynolds No.	9546	9525
Economizer		
Surface area, cm^2	1.0×10^6	1.0×10^6
Hydraulic diameter, cm	1.27	-
Number of equivalent channels	10347	-
Length, cm	24.2	26
Coolant temperature at entrance, °C	393	393
Surface temperature at entrance, °C	300	300
Average velocity, cm/sec	1258	1258
Average Reynolds No.	9039	9033

[a] From Ref. 16.

for the circulator, it was simply modeled by adding 12 m to the length of the cold ducting thereby giving an equivalent amount of surface area.

The PAD code requires essentially constant operating conditions. The calculations were done for 95% power and 105% flow and in EFPD time rather than real time. Most of the plant operating parameters were obtained from the FHSR (Ref. 9). The steam generator surface temperature distribution, shown in Fig. 21, was taken from the C. F. Braun design report (Ref. 17). The Braun calculations were based on a uniform shell-side helium distribution; however, the axial plateout distribution strongly suggests a helium maldistribution in the superheater section. Therefore, the actual surface temperature distribution in the superheater was probably somewhat different than that assumed; the magnitude of the effect is mitigated by the fact the tube-side thermal conductances were larger than the shell-side conductances so that the surface temperatures closely tracked the steam temperatures (Ref. 17).

The experimental cesium profiles in the steam generator have a clearly three-dimensional character, as is evidenced in Figs. 16 through 19. Since PAD models only one spatial dimension, the experimental profiles must also be collapsed to one dimension; this was accomplished by axially averaging the specific activity (along the 6-m length of the tube) and then averaging all the scanned tubes at a given radius (depth of penetration into the bundle); for example, those five tubes on the leading edge of the evaporator outlet (tubes EVO-102, -170, -170-1, -179, and -179-1 from Fig. 17) were lumped together as a single point.

The complete experimental and predicted cesium plateout distributions are compared in Fig. 22, the format of which is the PAD code representation of the Peach Bottom primary circuit; all the IRT data are displayed therein - the collapsed steam generator data along with the duct scans. The specific activity is plotted as a function of fractional cumulative surface area. (Note that the abscissa is drawn to scale within a given section but differs from one section to another.) Two PAD calculations are shown: (1) mass transfer control (i.e., the surfaces are perfect sinks for cesium), and (2) sorptivity control (adsorption isotherms are used to describe the sorptive

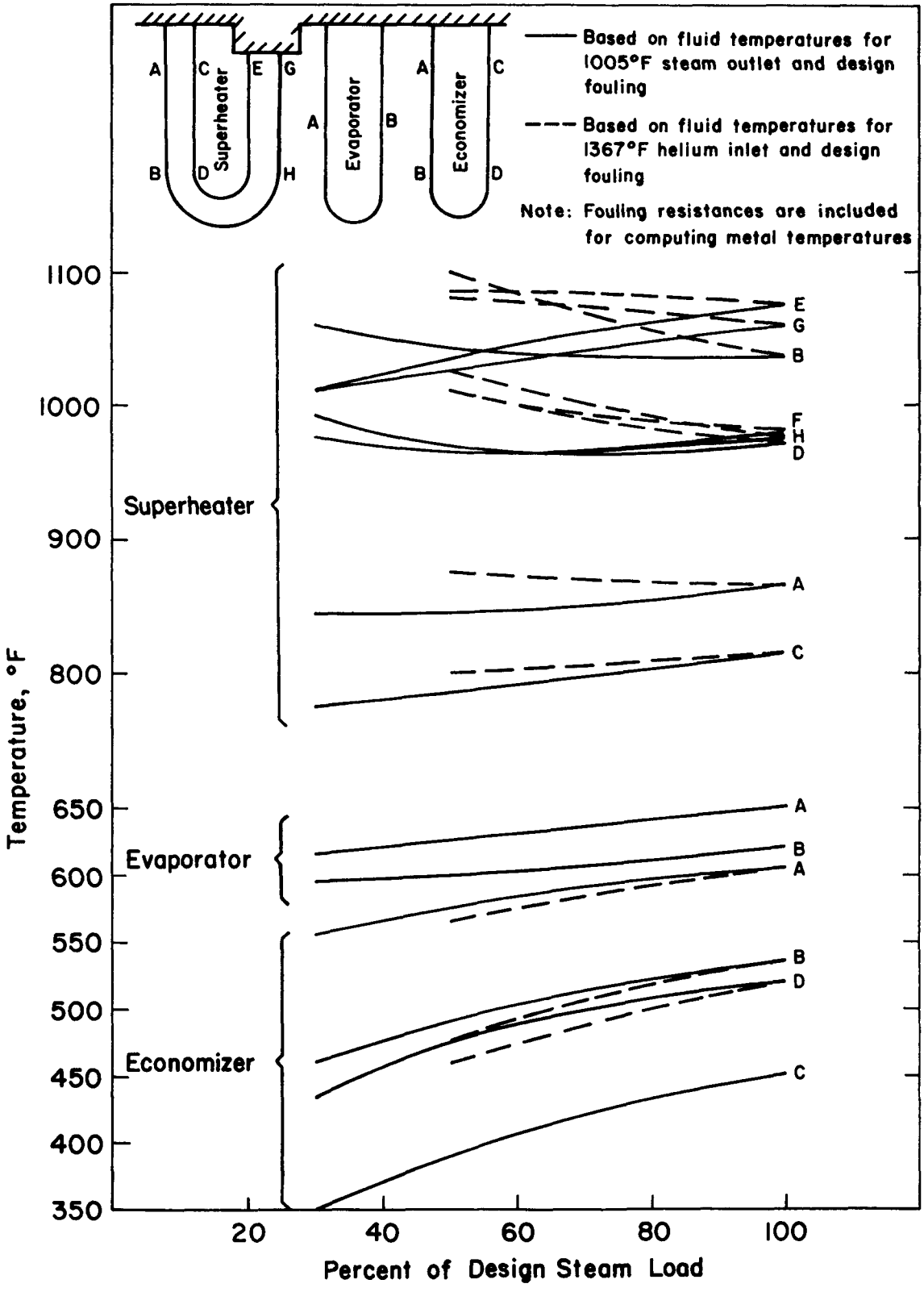

Fig. 21. Average tube metal temperatures

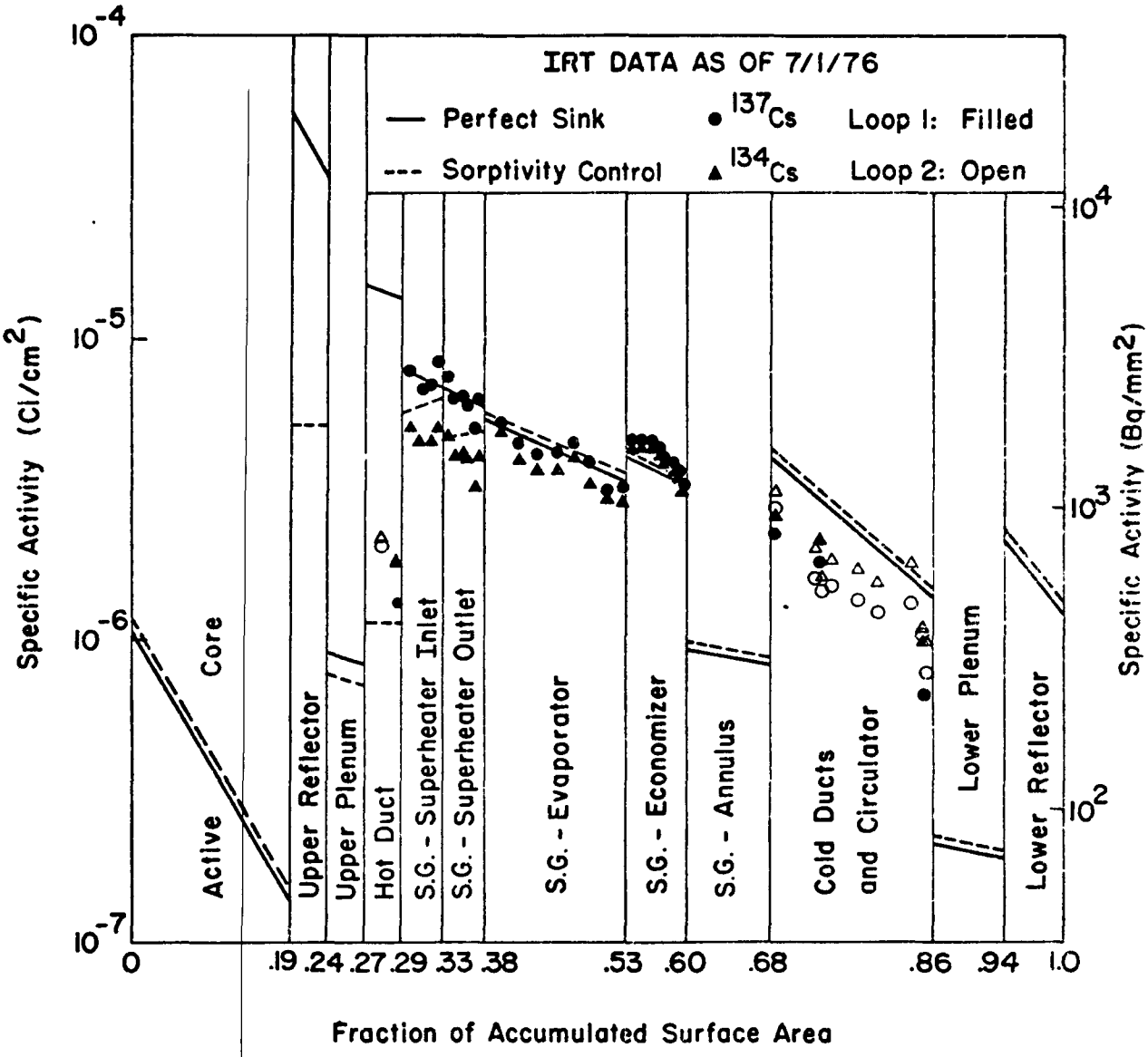

Fig. 22. Plateout distribution of Cs-137 and Cs-134 in Peach Bottom HTGR

capacity of the surfaces). The implications of these two cases are discussed at length below. In both cases the time-average, core release rate of cesium was adjusted so that the predicted specific activity at the evaporator inlet (shell-side) was approximately equal to the measured value ($\sim$5 $\mu Ci/cm^2$). Since the decay of Xe-137 produced negligible amounts of Cs-137 compared to the directly released component, the relative distributions shown in Fig. 22 apply equally well to Cs-134 which has no gaseous precursor.

The experimental plateout measurements from the cold ducts are shown in greater detail in Fig. 23 along with the predicted profile (here the perfect sink and sorptivity control cases are identical). The IRT data are shown together with the ORNL end-of-life external scans (Ref. 12) and the gamma scans of the destructively removed trepan samples. The data bars signifying the IRT internal scans represent some 20 to 40 individual scans (Fig. 20). Although there is some scatter, the three data sets appear consistent, and the least-squares line through the data has about the predicted slope. Both the IRT and ORNL external scans at the 100-m location (locations IRT-2-11 and ORNL-7, respectively) appear to be erroneously high; from Fig. 13, this location is near the bottom head of the steam generator, and some extraneous contribution from that source is suspected.

Inspection of Fig. 22 indicates that the mass transfer control, or perfect sink, case (solid lines) resulted in good agreement everywhere except in the hot duct leading from the reactor vessel to the steam generator. Here the specific cesium activity is overpredicted by an order of magnitude. Since the flow geometry is simple (a circular duct), prediction of the mass transfer coefficient should be reasonably accurate. Thus, the logical conclusion is that the deposition process in the hot duct is not limited by mass transfer effects. As discussed in Appendix B, surfaces are known to have a limited sorptive capacity for cesium at high temperatures; therefore, this behavior was not unexpected. The problem then was the choice of an appropriate sorption isotherm to describe this effect.

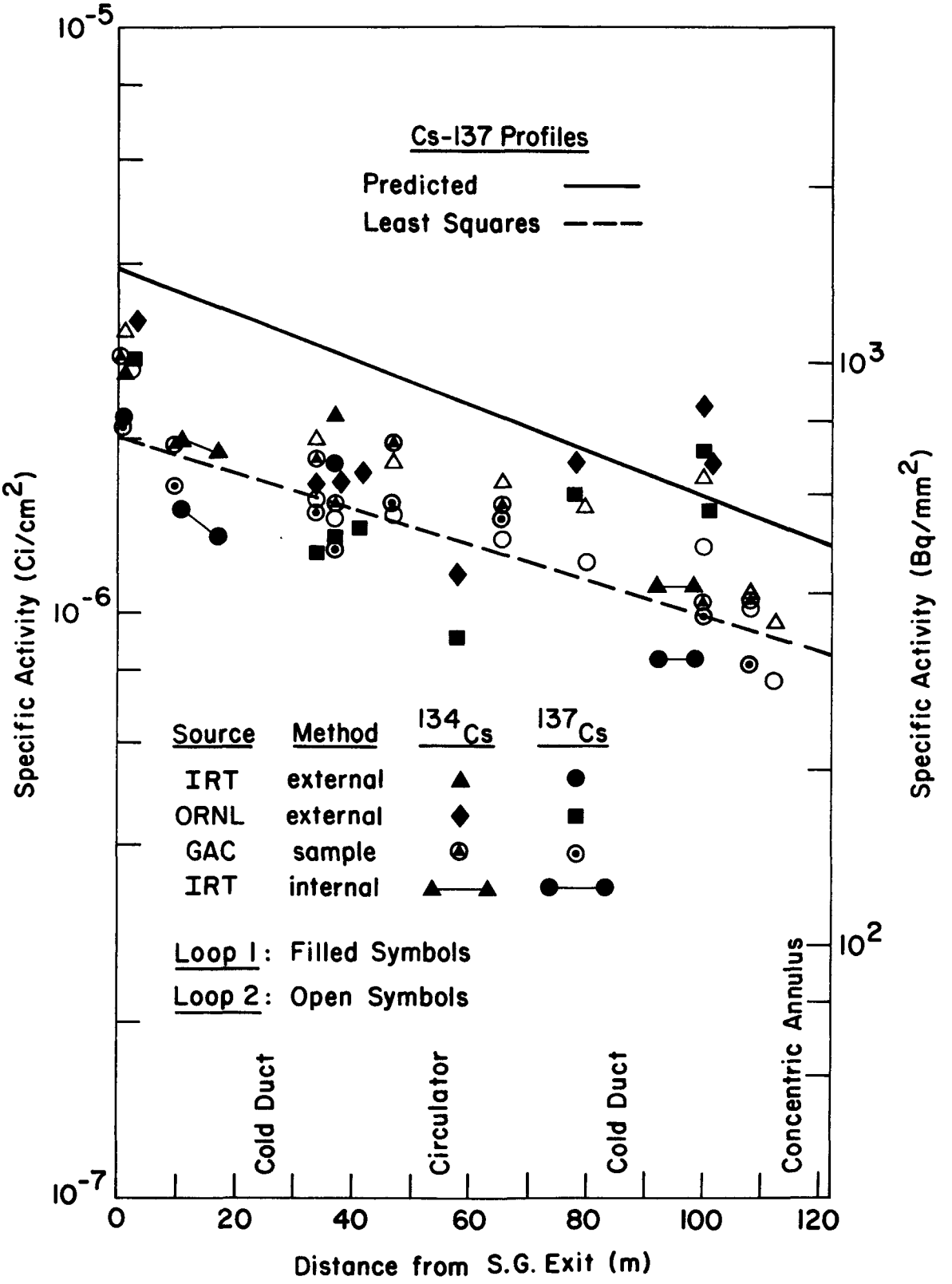

Fig. 23. Cesium deposition profiles in cold duct

The cesium sorptivity of metallic surfaces is not well defined. For SS-304, the hot duct material, the oxidation state of the surface has a profound effect with pre-oxidation favoring increased sorption (Refs. 18, 19). For Incoloy 800, the superheater material, very little data have been published; however, it appears to be substantially less sorptive than oxidized SS-304, but not unlike as-received SS-304 (Fig. B-1) at the temperatures of interest for the superheater (~700°K) according to Ref. 20. Further, the cesium sorptivity of Incoloy 800 was also found to be enhanced by surface oxidation.

Since the oxidation state of the hot leg surfaces was unknown, a parametric study was performed, taking the sorptivity of oxidized SS-304 as the base case. A four-constant Freundlich isotherm was generated from the data in Fig. B-2; for expediency this isotherm was also used for the Incoloy 800 superheater since the Incoloy 800 data from Ref. 20 have not yet been reduced. The carbon steel surfaces were assumed to be perfect sinks because of the low temperatures and their large cesium sorptive capacities (Ref. 18). The axial-average, entrance and exit surface temperatures for the superheater inlet and outlet sections were computed from the Braun design temperatures (Fig. 21). The cesium plateout distribution calculated with this isotherm was identical to the perfect sink case; i.e., the cesium sorptivity was overpredicted. The sorptivity relative to oxidized SS-304 was then progressively reduced until approximately the measured hot duct specific activity was obtained. The dashed lines in Figs. 22 and 24 correspond to the case where the sorptivity is 1/20 that of oxidized SS-304; with this case, the specific activity in the hot duct is underpredicted by a factor of about 2, and the sorption effects in the superheater section are modest (almost all the cesium that was transferred to the surface - the solid lines - was accommodated). If the relative sorptivity is raised to 1/10 the base case, then the specific activity in the hot duct is increased by a factor of 2 giving the measured result, and the superheater becomes a perfect sink (dotted line in Fig. 24). This final case matches the measured distribution almost exactly.

As described previously, all exposed surfaces in the primary circuit were covered with a carbonaceous deposit produced by cracking of lubricating

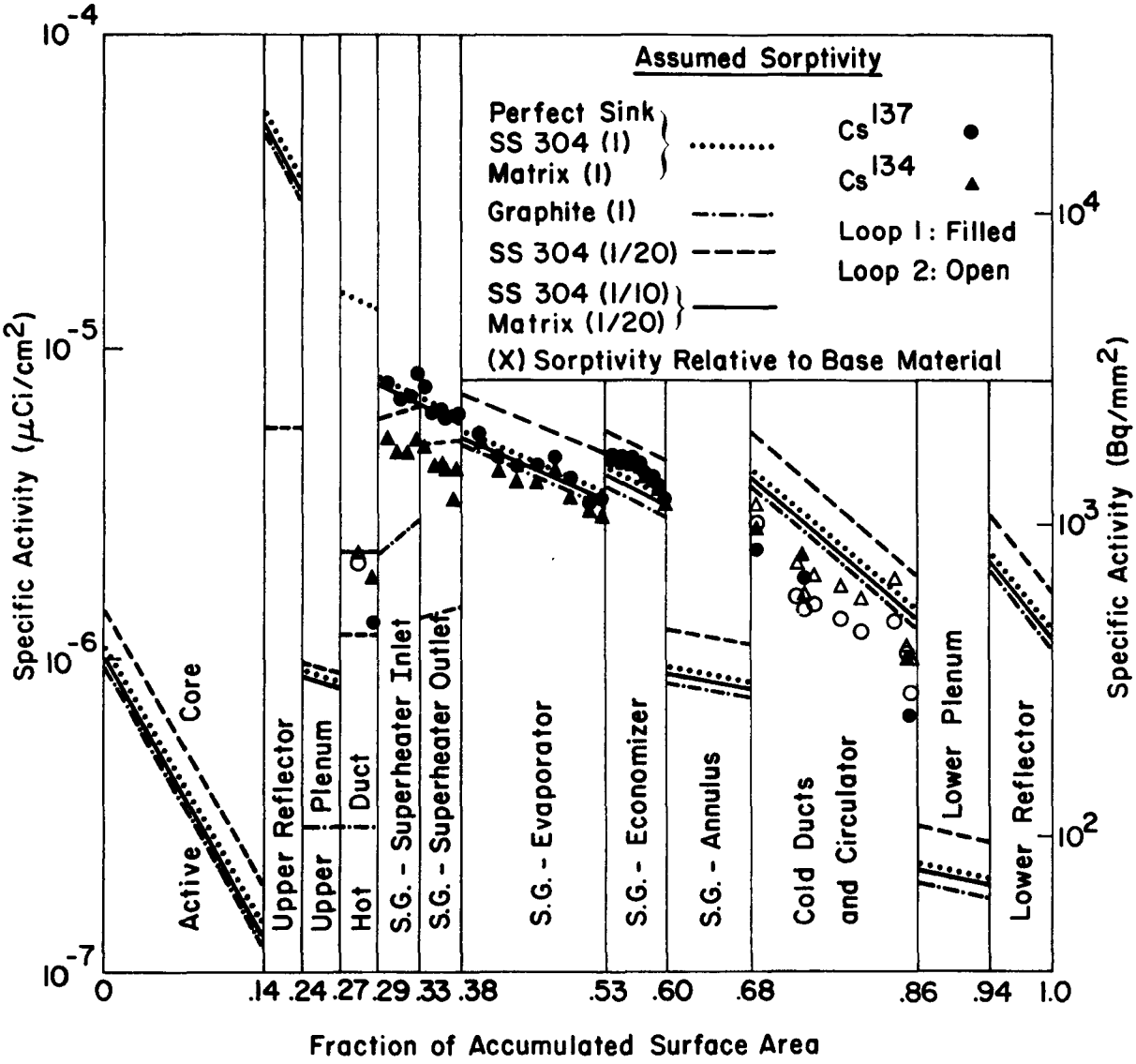

Fig. 24. Effect of surface sorptivity on cesium plateout distribution

oil which had leaked into the primary circuit. This carbon deposit was possibly a significant sink for cesium. Conceivably then, the plateout surfaces may be more appropriately characterized as being carbonaceous rather than metallic; this possibility was also investigated parametrically.

The physical and chemical characteristics of this carbon deposit are still being determined at GA and ORNL. Presently, it is known to range from about 6 to 12 μm in thickness and to be 80 to 90% carbon with up to 10% iron and detectable amounts of sulfur and silicon (Ref. 12). Little is known about the structure; this is unfortunate because the cesium sorptivity of carbon substances is strongly structure-dependent. For example, the HTGR fuel rod matrix (a coke, or char, from the pyrolysis of coal tar pitch) is substantially more sorptive than is graphite (Ref. 21); since the cesium sorptivities of these materials have been characterized (sorption isotherms are given in Appendix A), they may be useful in judging the importance of the carbon deposits in Peach Bottom.

A number of assumptions had to be made to apply these data. First, the average deposit thickness was taken as 10 μm and a unit density (1 g/cm^3) was assumed. If the deposit resembled graphite, then the BET internal surface area was of the order of 1 m^2/g. With these assumptions, every square centimeter of geometric surface in the circuit was equivalent to 1 mg, or 10 cm^2 (BET), of graphite. Since the PAD code considers only geometric surface area, it was necessary to artificially increase the cesium sorptivity predicted with the graphite isotherm by a factor of ten. As shown in Fig. 24, the hot duct cesium concentrations were underpredicted by almost an order of magnitude when assuming the sorptivity of graphite.

A similar procedure was followed in applying the cesium-on-matrix isotherm; however, in this case, the BET surface area was taken to be 10 m^2/g, giving a correction factor of 100 cm^2 (BET)/cm^2 (geom.). The result is prediction of perfect sink plateout behavior, or an overestimation of cesium sorptivity. However, if the sorptivity is reduced by a factor of 20 relative to the matrix case, then the experimental profile is matched almost exactly (Fig. 24), as was the case with the SS-304 isotherm and a relative sorptivity of 1/10.

In summary, the experimentally observed cesium plateout distribution in Peach Bottom can be predicted almost exactly with the PAD code providing appropriate sorption isotherms are employed. However, the observed sorption behavior is consistent with either assuming that the primary cesium sink is a relatively oxide-free surface or assuming that the carbon deposit has a cesium sorptivity intermediate to that of graphite and matrix. The assumptions are equally feasible; in reality, both probably contributed to the total sorptive capacity of the surface.

The major reason that sorption effects were apparently limited to the hot duct is that surface temperatures in the superheater were relatively low, as intended, because of the cocurrent flow design. However, axial-average temperatures were used in the above calculations, and the experimental profiles are also averages. Hence, some modest temperature effects, i.e., sorption effects, in the superheater might have been masked. To investigate this possibility, radial (across the bundle) profiles were computed at the top, near the midplane, and at the bottom of the tube bundle (sections aa, bb, and cc, respectively in Fig. 2). These profiles are shown in Fig. 25 along with the surface temperature distributions at these elevations. Also shown for each elevation are predicted cesium profiles for mass transfer control (dashed line) and sorptivity control (SS-304 isotherm with a 1/20 relative sorptivity). These predictions are analogous to the average predictions in Fig. 22; again, increasing the relative sorptivity to 1/10 would give the perfect sink case in the superheater (assuming matrix temperature dependence and a relative sorptivity of 1/20 gives identical results). By inspection, there are apparently no sorption effects. However, the specific activity, if not the slope of the profile, varies at the three elevations in the superheater (but not in the evaporator and economizer sections). This is a consequence of the superheater flow maldistribution which is more clearly demonstrated in Fig. 19. Since the predicted slope of the profile (in the perfect sink case) is only slightly dependent upon the mass flow rate (slope $\alpha\ \dot{m}^{0.17}$), a change in the mass flow rate would simply displace the profile relative to the uniform flow profile in proportion to the ratio of the flow rates.

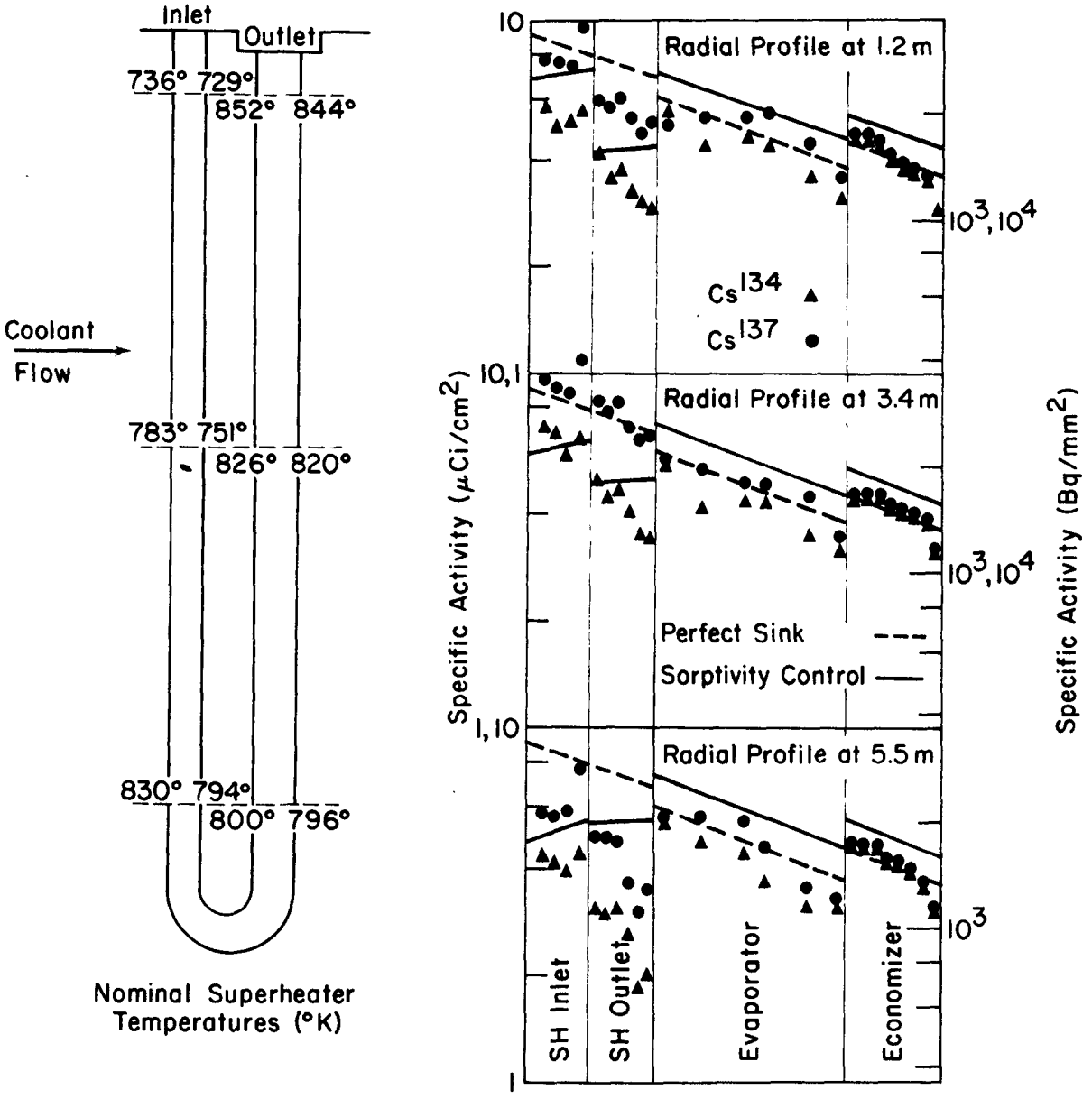

Fig. 25. Effect of superheater temperature distribution

4. DISCUSSION

Overall, this design methods verification program has been remarkably successful. While the most satisfying aspect is the excellent agreement between the measured and predicted cesium plateout distribution, there were other notable accomplishments as well. The detectors and associated hardware were designed with only limited knowledge of the actual test environment and radiation intensities. Except for the initial difficulties with saturation of the CdTe detectors, the test equipment performed quite satisfactorily. Further, the entire program - data acquisition, reduction, and analysis - has been accomplished for essentially the original cost estimate (~$200,000) and reasonably on schedule (except for the delay to remedy the detector saturation problem). However, as with most experimental work, there are limitations to both the experimental and analytical methodology that merit discussion. In addition, it is currently impossible to give an unambiguous interpretation of the experimental results (these ambiguities may be resolved when on-going work at ORNL and GA is completed).

The most serious hardware problems were encountered with the CdTe detectors. The degree of miniaturization required, because of the small diameters of the tubes, necessitated compromising detector resolution, thereby complicating data reduction. Since subsequent Ge(Li) scans of removed specimens of tubes have confirmed that only Cs-137 and Cs-134 occurred in abundance, this marginal resolution was tolerable in this Peach Bottom scanning; it could be more serious in other applications.

The fact that the Cs-134 and Cs-137 peaks (0.605 and 0.662 MeV, respectively) were not completely resolved introduces additional uncertainty into the Cs-137 results; however, the Cs-137 results (based upon the 0.795-MeV peak) should be unaffected. Since the Cs-134 and Cs-137 profiles do not differ markedly, the numerical stripping techniques used

to obtain Cs-137 activities were apparently successful.

In addition, CdTe detectors inherently exhibit a low peak-to-Compton ratio at ambient temperatures which aggrevated the resolution problems and resulted in detector saturation with the early design. This latter problem was alleviated by tantalum shielding and faster electronics; however, inclusion of shielding made the physical dimensions too large for use in the economizer section, and this section had to be mapped with non-discriminate GM detectors.

While CdTe detectors do have limitations, they also have significant assets. It is doubtful that the Peach Bottom steam generator data could have been obtained with any other available type of detector. There may be numerous other applications where CdTe detectors could be exploited in the operational surveillance of power reactors. For instance, determination of radioactive "crud" levels [primarily Co-60 (Ref. 22)] in water-reactor steam generators might be a possibility.

Another limitation of the steam generator results is the number of assumptions in the calibration procedures. First, the geometry is complex and variable from tube to tube. For those tubes in the interior of the tube bundles, reasonable accuracy can be expected (±10%); however, for those tubes on the periphery, larger errors can be expected. For example, contributions from plateout on the tube bundle shroud were ignored. Similarly, the effects of the tube support and flow baffles were also ignored. Hence, the apparently large decreases in specific activity at the baffle plate elevations (Fig. 19) are probably overestimations. Some actual decrease is reasonable, however, since the amount of axial flow between the baffle and tube is probably small compared to the crossflow over the tubes.

With the above limitations, and possibly others as well, it is not unreasonable to expect significant errors in the steam generator scans. From Ref. 7 the estimated standard deviation is of the order of ±10% for the Cs-134 data

and ±20% for the Cs-137 data (the latter being larger because of the incomplete spectral resolution). However, these estimates could be optimistic, and the actual errors could easily be twice as large. A more rigorous assessment of experimental accuracy will be possible when the radiochemical examination of the destructively removed samples is completed. As seen in Fig. 23, the in situ duct scans and scans of the trepanned samples are in excellent agreement; initial scans of the tube samples are also encouraging.

The most serious difficulties in applying the PAD code to predict the plateout distribution were outlined in Section 3. In general, the most important considerations are the modeling of complex geometries and the choice of sorption isotherms. Normally, modeling the steam generator tube bundle would have been anticipated as presenting the greatest modeling problem; however, since the slopes of the predicted and measured profiles are consistent, the PAD representation was apparently adequate. From Fig. 23, the specific activity in the cold duct is overpredicted by a factor of about two even though the slope is nearly correct. One explanation is that the amount of plateout, hence depletion of cesium from the coolant, in the annulus between the steam generator tube bundle shroud and shell was underpredicted. Since no plateout data exist for this section, the speculation can not be confirmed. Similarly, no data exist for the upper and lower plenum sections. However, most of the plateout surface area is in the tube bundles and ducting, and there the modeling appears adequate.

Also, as discussed previously, the cesium sorptivity of HTGR structural materials has not been well characterized. Therefore, this important variable had to be investigated parametrically. To some extent then, the good agreement between predicted and measured cesium distributions might be judged as inspired curve fitting. While this possibility can not be eliminated completely, the apparent sorptivities deduced from the experimental profiles are not inconsistent with the limited available sorption data. The observed profile can be obtained by assuming that the metal surfaces are the primary cesium sink and assigning them a sorptivity

one-tenth that of the oxidized SS-304. Given the high H_2/H_2O ratio in the coolant throughout Peach Bottom operation (Ref. 11), the metal surfaces should have been relatively "oxide free." The observed profiles can also be obtained by assuming the primary sink to be the carbon deposit with a sorptivity intermediate to that of graphite and fuel rod matrix which is certainly not unreasonable.

It is currently impossible to conclude unequivocally the extent to which the carbon deposit enhanced the cesium sorptive capacity of the hottest surfaces of the primary circuit. During the examination of the removed samples from the hot duct and the superheater tubes, it was observed that some of the carbon deposit was easily dislodged from the sample and that this "fallout" was highly contaminated. Clearly then, the carbon deposit was a cesium sink, but the relative distribution of the deposit and the base metal is still unknown. Decontamination studies currently in progress may provide further insight.

The ubiquituous presence of carbon dust also might have been expected to complicate the mass transfer process as well, by introducing the prospect that the cesium might be transported on dust rather than as an atomic species. That some cesium-on-dust transport did occur is known from the ORNL diffusion probe studies and analysis of dust collected in the centrifugal separators (Ref. 12). However, since the cesium profiles in the tube bundle and cold duct have slopes consistent with PAD predictions, the logical conclusion is that the preponderance of the deposited cesium was transported in molecular form.

Despite uncertainties in both the measurements and the predictions, and despite the complications introduced by the carbon dust, the agreement between the PAD code calculations and the in situ gamma scans is remarkably good. Questions of mechanism aside, the agreement suggests that the PAD code is an adequate empirical tool for predicting plateout distributions provided appropriate sorption isotherms are available. By induction, this success tends to verify the reference methodology used to make such predictions for large HTGR design.

APPENDIX A

REVIEW OF THE MATHEMATICAL MODEL EMPLOYED BY THE PAD CODE

The mathematical model employed by the PAD code is thoroughly documented in Ref. 2; however, for convenience, certain sections of that document are excerpted below.

A.1. CONSERVATION EQUATIONS

The conservation equations presented here describe the mass balance for the coolant and surface fission product concentrations in sections of the reactor circuit with constant cross-sectional areas. The treatment is a simplified analysis giving surface concentrations and average coolant concentrations as a function of axial distance and time. It is assumed that the mass-transport process can be described to be between an average coolant concentration and a surface concentration separated by a thin gaseous boundary layer film. The quantity of fission products contained in the thin film is assumed to be negligible. Figure A-1 illustrates the basic mass-transport volume element.

The coolant and surface concentrations of each fission product are dependent on a source term, such as the release of the fission product from the reactor core, on the decay of the parent fission product in the primary circuit, on the decay of the fission product itself, on mass transfer between the coolant and surface, and on axial convection around the reactor circuit. Hence, the time rate of change of the amount of fission product j in an increment of volume of length dx, cross-sectional area A, and wetted perimeter P is given by

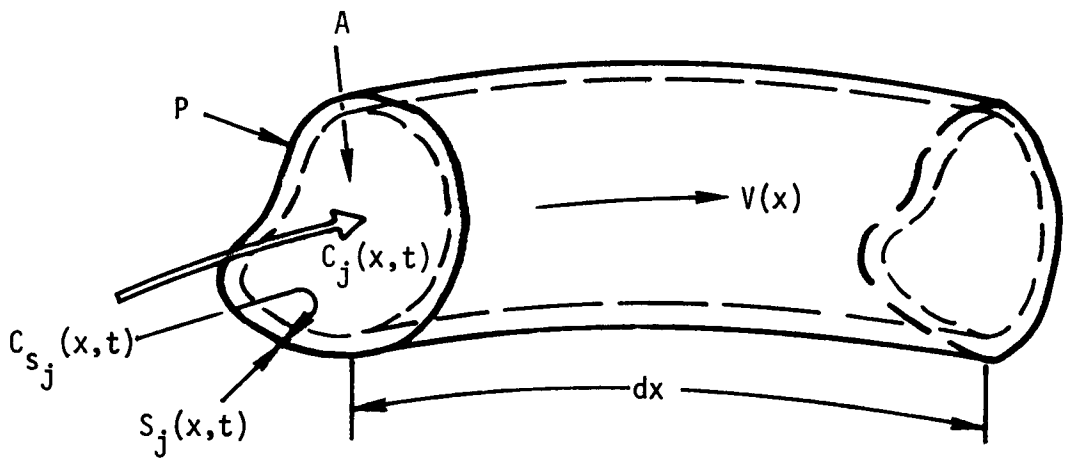

Fig. A-1. Basic mass-transport volume element

$$\frac{\partial C_j(x,t)}{\partial t} Adx = \underbrace{B_j(x)Adx}_{\text{Source term}} + \underbrace{\lambda_i C_i(x,t)Adx}_{\text{Decay from parent}} - \underbrace{\lambda_j C_j(x,t)Adx}_{\text{Decay}}$$

$$- \underbrace{\left[\left(V(x)C_j(x,t) + \frac{\partial[V(x)C_j(x,t)]}{\partial x}\right)dx \quad A - V(x)C_j(x,t)Adx\right]}_{\text{Flow out of increment - flow in = loss rate due to axial convection}}$$

$$\underbrace{- k(x)[C_j(x,t) - C_{s_j}(x,t)]Pdx}_{\text{Mass transfer from average coolant concentration to coolant concentration at the surface}} . \qquad \text{(A-1)}$$

or,

$$\frac{\partial C_j(x,t)}{\partial t} = B_j(x) + \lambda_i C_i(x,t) - \lambda_j C_j(x,t) - \frac{\partial[V(x)C_j(x,t)]}{\partial x}$$

$$- \frac{k(x)P}{A} [C_j(x,t) - C_{s_j}(x,t)] \quad , \qquad \text{(A-2)}$$

where $C_j(x,t)$, $C_i(x,t)$ = coolant concentration of fission product j and its precursor i averaged across the coolant channel, $\mu g/cm^3$,

$C_{s_j}(x,t)$ = coolant concentration of fission product j at the channel surface, $\mu g/cm^2$,

x = axial distance coordinate, cm,

t = time coordinate, sec,

$B_j(x)$ = source of fission product j in the coolant, $\mu g/cm^3$-sec,

λ_j, λ_i = decay constant of fission product j and its precursor i, sec^{-1},

$V(x)$ = velocity of coolant, cm/sec,

P/A = ratio of wetted perimeter to cross-sectional area of coolant channel, cm^{-1},

$k(x)$ = mass-transfer coefficient, cm/sec.

Similarly, the time rate of change of the amount of fission product j on a surface element of length dx and wetted perimeter P is given by

$$\frac{\partial S_j(x,t)}{\partial t} Pdx = \underbrace{b_j(x)Pdx}_{\text{Source term}} + \underbrace{\lambda_i S_i(x,t)Pdx}_{\text{Decay from parent}} - \underbrace{\lambda_j S_j(x,t)Pdx}_{\text{Decay}}$$

$$+ \underbrace{k(x)[C_j(x,t) - C_{s_j}(x,t)]Pdx}_{\substack{\text{Mass transfer from average coolant concentration to coolant concentration at the surface}}} . \qquad \text{(A-3)}$$

or,

$$\frac{\partial S_j(x,t)}{\partial t} = b_j(x) + \lambda_i S_i(x,t) - \lambda_j S_j(x,t)$$

$$+ k(x)[C_j(x,t) - C_{s_j}(x,t)] \quad , \qquad \text{(A-4)}$$

where $S_j(x,t)$, $S_i(x,t)$ = surface concentration of fission product j and its precursor i, $\mu g/cm^2$,

$b_j(x)$ = source of fission product j on the surface, $\mu g/cm^2$-sec,

and the remainder of the terms are as previously defined. Equations A-2 and A-4 control the behavior of fission product j within one section of the reactor circuit. A similar set of equations must be written for each reactor section in order to completely describe the behavior of fission project j throughout the reactor circuit. The initial and boundary conditions are: (1) the initial concentrations are specified and (2) the coolant concentration is continuous around the reactor circuit.

A.2. MASS-TRANSFER COEFFICIENT

The mass-transfer coefficient k(x) used in Eqs. A-2 and A-4 should be for mass transfer in a turbulently flowing gas stream through a channel of constant cross-sectional area. A formulation for channels of circular cross-section is given by

$$k(x) = [0.023\ D(x)/d]\ [Re(x)]^{0.83}\ [Sc(x)]^{0.44} \quad , \qquad \text{(A-5)}$$

where D(x) = diffusion coefficient of species in gas stream, cm^2/sec,

d = diameter of circular conduit, cm,

$Re(x)$ = Reynolds number of gas stream,

$Sc(x)$ = Schmidt number of gas stream.

Although this expression is primarily for channels of circular cross-section, other shapes can be accommodated by using the hydraulic diameter.

A.3. SURFACE SORPTION

In order to relate the coolant concentration at the surface, $C_s(x,t)$, to the surface concentration, $S(x,t)$, an algebraic expression for the surface sorption equilibrium is needed. Several equations have been found to approximate a large amount of the experimental isotherm data on equilibrium partial pressures versus surface loading. One of these, the Freundlich equation, can be written as

$$C_s(x,t) = K_f(x)\ S(x,t)^{n(x)} \quad , \tag{A-6}$$

where $K_f(x)$ = the temperature-dependent Freundlich sorption constant relating desorption and adsorption coefficients,

$n(x)$ = the temperature-dependent constant which has been observed to be greater than one.

Although this expression is an empirical equation, it is sufficient for describing much of the experimental data.

Another expression, the Langmuir equation, can be written as

$$C_s(x,t) = K_\ell(x) \left(\frac{S(x,t)}{1 - S(x,t)/S_{sat}} \right) \quad , \tag{A-7}$$

where $K_\ell(x)$ = the temperature-dependent Langmuir sorption constant relating desorption and adsorption coefficients,

S_{sat} = saturated surface concentration.

This expression was deduced from a definite hypothesis on the mechanism of the sorption process, i.e., that the rate of sorption is dependent on the number of unoccupied surface sites. As the surface concentration approaches the saturated surface concentration, the number of sorption sites becomes vanishingly small, resulting in a rapid increase of the coolant concentration above the surface. Note that at low coverage values the coolant concentration becomes linearly proportional to the surface concentration.

A general expression that results in either equation, depending on the values of the constants, can be written as

$$C_s(x,t) = K(x) \left[\frac{S(x,t)^{n(x)}}{1 - \delta_{n1} S(x,t)/S_{sat}} \right] , \qquad \text{(A-8)}$$

where δ_{n1} = Kronecker delta function,

$\delta_{n1} = 1$ if $n = 1$,

$\delta_{n1} = 0$ if $n \neq 1$.

Since there may be many isotopes of the same chemical species sorbed on the surface, one must consider the surface concentration of each isotope with relation to the total surface concentration of all the isotopes of the same chemical species. Therefore, the surface concentration terms in Eq. A-8 must be summed over all isotopes of the same chemical species and the expression multiplied by the mole fraction of isotope j to obtain the proper concentration for isotope j. Hence, Eq. A-8 becomes

$$C_{s_j}(x,t) = K(x) \left[\frac{[\Sigma S(x,t)]^{n(x)}}{1 - \delta_{n1} \Sigma S(x,t)/S_{sat}} \right] \frac{S_j(x,t)}{\Sigma S(x,t)} . \qquad \text{(A-9)}$$

Generally, different chemical species can be included in the summation by using weighted values of the constants and concentrations in Eq. A-9.

In order to keep the theoretical treatment relatively simple and straightforward, the explicit temperature dependence of the sorption constants in Eqs. A-6, A-7, and A-8 has been suppressed. However, most of the experimental sorption data are reported in a form that explicitly shows this temperature dependence. The code input has therefore been designed to accept these experimental constants. This is accomplished by calculating the coolant concentration at the surface for either the Freundlich or the Langmuir type of sorption kinetics from an equation of the form

$$C_s(x,t) = \frac{\exp\,[ACP+BCP\cdot 10^3/T(x)]\; S(x,t)^{(CCP+DCP\cdot 10^3/T(x))}}{[1-S(x,t)/DCP\cdot 10^{23}]} \quad , \qquad \text{(A-10)}$$

where $T(x)$ = the absolute temperature of the surface, °K,

$S(x,t)$ = the surface concentration of the sorbed species (units vary with experiment),

and ACP, BCP, CCP, DCP are constants. Hence, the expressions for $K(x)$ and $N(X)$ in Eq. A-8 are, respectively,

$$K(x) = \exp\,[ACP+BCP \cdot 10^3/T(x)] \quad ,$$

$$n(x) = CCP+DCP \cdot 10^3/T(x) \quad . \qquad \text{(A-11)}$$

For Freundlich-type behavior, all the constants are determined from the experimental data (the denominator will be approximately equal to one). For Langmuir-type behavior, the constant CCP is set equal to one, the constant DCP is set equal to the product of 10^{-23} and the saturated surface concentration S_{sat}, and the constants ACP and BCP are determined from the experimental data. Note that this procedure is numerically equivalent to the Kronecker delta formulation given in Eq. A-8. Of course, the surface concentration terms in Eq. A-10 should be summed over all isotopes of the same chemical species and the result multiplied by the mole fraction of the isotope under consideration (see Eq. A-9).

In addition to simple Freundlich or simple Langmuir sorption kinetics, certain systems exhibit Freundlich-type behavior at the higher surface concentrations and Langmuir-type behavior at lower concentrations; that is, the gaseous concentration becomes proportional to the surface concentration at the lower surface loadings. The proportionality constant is determined by evaluating the gaseous concentration at the critical surface loading, CRITSC, and then dividing by the critical loading. The program will automatically make this change in sorption behavior if a critical surface loading, CRITSC, is supplied.

A.4. SORPTION ISOTHERMS

The sorption isotherms used in this study were reported in Ref. 15 and those results are summarized in Table A-1.

TABLE A-1

CESIUM SORPTION ISOTHERMS[a]

System	Isotherm Constants[b]				Concentration Units	CRITSC[c]
	ACP	BCP	CCP	DCP		
Matrix	8.39	-38.3	-0.50	4.10	μmole/g	4.0
Graphite	7.09	-27.6	-0.50	4.10	μmole/g	0.3
Oxidized SS-304	74.84	-100.1	-37.82	43.12	$\mu g/cm^2$	-

[a] From Ref. 15.

[b] Constants in Eq. A-11.

[c] Concentration at which transition to Henrian behavior is presumed to occur.

APPENDIX B

SORPTIVITY EFFECTS IN THE PREDICTION OF CESIUM PLATEOUT DISTRIBUTION

There is ample evidence demonstrating that graphitic and metallic surfaces have a limited capacity for sorbing cesium at elevated temperatures; the difficulty is in quantifying the effect (Ref. 15). Graphite is a porous material having a BET internal surface area of the order of 1 m^2/g; the question then becomes the availability of this internal surface area in graphite structures such as reflectors to sorb cesium. In other words, the sorption process for graphite involves solid-state diffusion as well as adsorption. Since a rigorous analysis has not yet been performed, it is currently assumed (for conservatism) that all of the internal surface area is accessible for sorbing cesium; this may, in fact, grossly overestimate the sorptive capacity of graphite structures.

The difficulty regarding the cesium sorptivity of metal surfaces is somewhat different. The diffusion of cesium into metals is probably an insignificant effect at temperatures of interest for Peach Bottom (<700°C). A more serious problem is the oxidation state of the surface; its effect on the cesium sorptivity of 304 stainless steel (the thermal barrier material in Peach Bottom) has been convincingly demonstrated by Zumwalt and Milstead (Refs. 18, 19). When a specimen was preoxidized by exposure to air at 625°C for 18 hours, the amount of cesium sorbed at a given partial pressure and surface temperature increased by a factor of 40 to 60 over that of an "as-received" specimen; the effect is illustrated in Figs. B-1 and B-2 (Ref. 19). This apparent surface chemistry effect also suggests that different metals should have different cesium sorptivities. A further complication in the case of Peach Bottom is the ubiquitious presence of carbonaceous deposits throughout the primary circuit; a major, if not

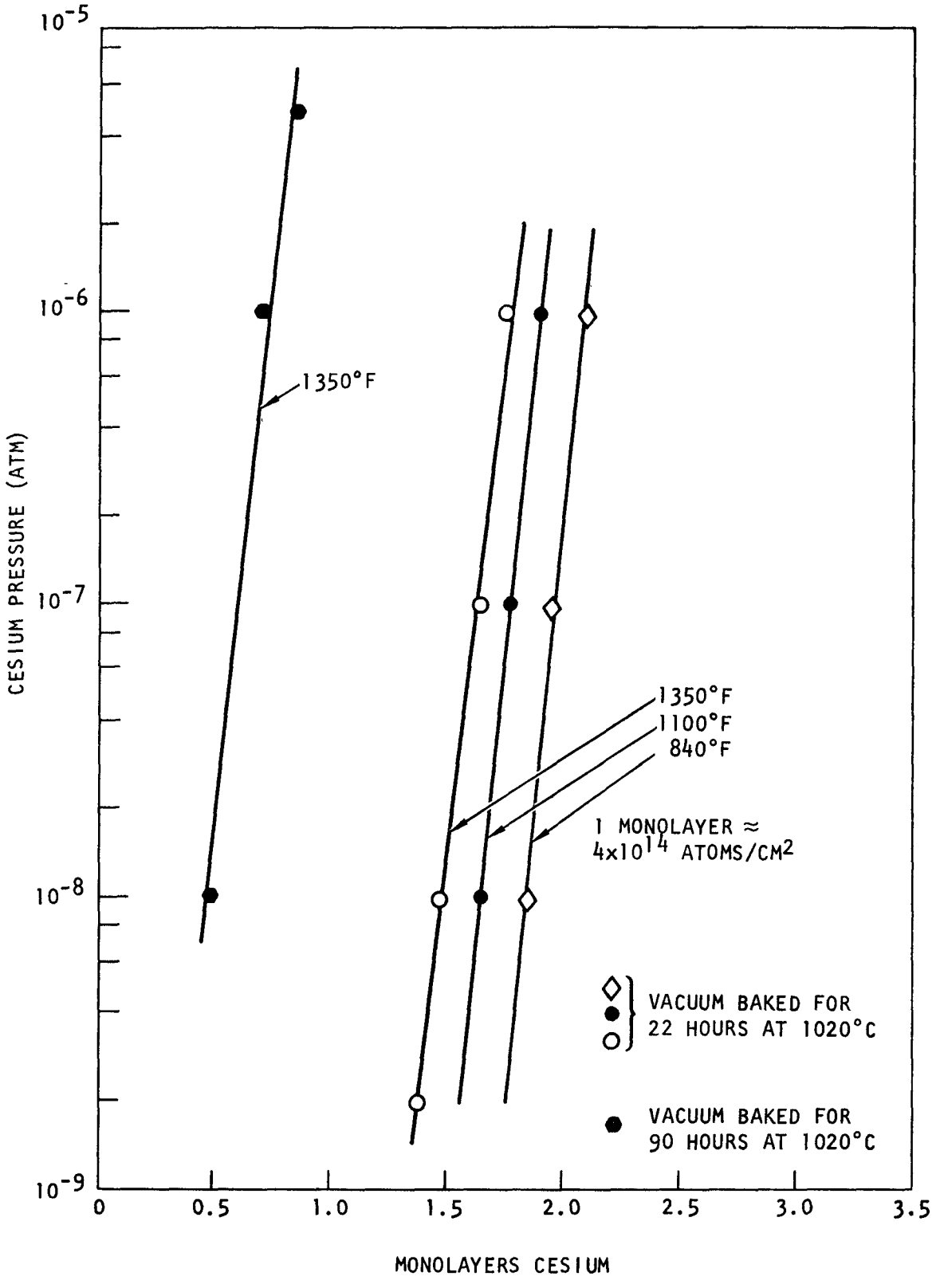

Fig. B-1. Deposition of cesium on 304 stainless steel

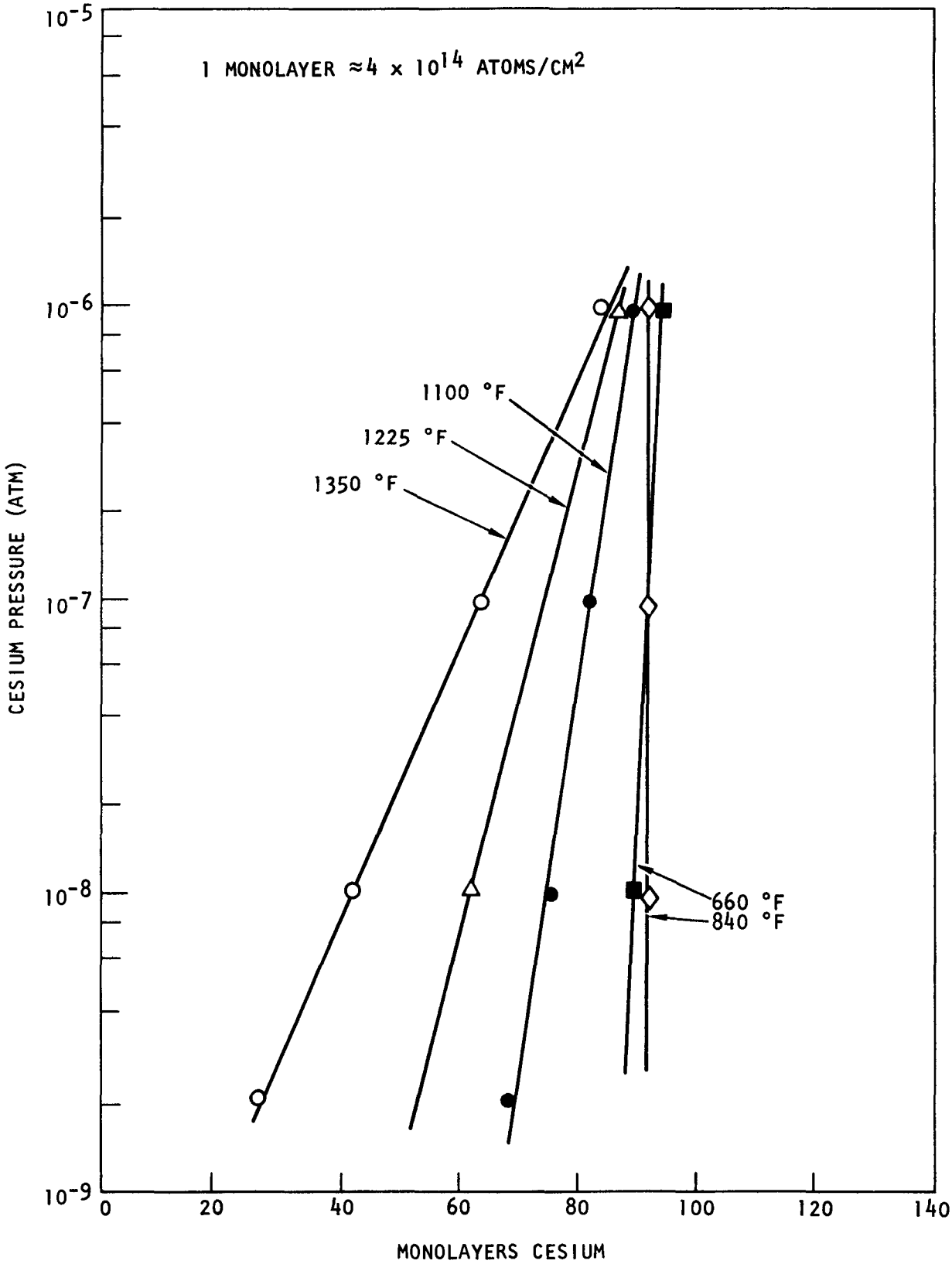

Fig. B-2. Deposition of cesium on oxidized 304 stainless steel

exclusive, source of these deposits was the cracking of lubricating oil which intermittently leaked into the primary coolant from the purified helium transfer compressors (Ref. 11). Depending upon their physical characteristics, these carbon deposits could be an important sink for cesium.

REFERENCES

1. "Work Plan for Peach Bottom End-of-Life Program," General Atomic unpublished data, August 15, 1975.

2. Vanslager, F. E., and L. D. Mears, "PAD: A Computer Code for Calculating the Plateout Activity Distribution in a Reactor Circuit," Gulf General Atomic Report GA-10460, January 1971.

3. Hanson, D. L., "Test Specification: Phase I Gamma Scanning of the Peach Bottom Primary Circuit," General Atomic unpublished data, July 25, 1975.

4. Hanson, D. L., "Test Specification: Phase 2 Internal Gamma Scanning of the Peach Bottom Primary Circuit," General Atomic unpublished data, October 28, 1975.

5. "Test Procedure for Gamma Scanning the Peach Bottom Primary Circuit: Phase 1 - External Scans," IRT Corporation Report 167-56-9, June 1, 1975.

6. "Test Procedure for Gamma Scanning the Peach Bottom Primary Circuit: Phase 2 - Internal Scans," IRT Corporation Report 167-56-10, November 1, 1975.

7. Selph, W. E., and D. E. Bryan, "Measurement of Fission Product Activity in the Peach Bottom Reactor Primary Coolant Loop," IRT 0029-001, Intelcom Rad Tech Corporation Report IRT 0029-001, June 1976 (also ERDA Report GA-A14059, General Atomic Company, August 1976).

8. Hanson, D. L., "Work Plan for the Design Methods Verification Subtask of the Peach Bottom End-of-Life Program," General Atomic unpublished data, July 9, 1976.

9. "Peach Bottom Atomic Power Station, Final Hazards Summary Report," Philadelphia Electric Company.

10. "Planning Guide for HTGR Safety and Safety-Related Research and Development," Appendix B, USAEC Report ORNL-4968, Oak Ridge National Laboratory, May 1974.

11. Scheffel, W. J., N. L. Baldwin, and R. W. Tomlin, "Operating History Report for the Peach Bottom HTGR," Volume 1, ERDA Report GA-A13907-1, General Atomic Company, August 31, 1976.

12. Dyer, F. F., et. al., "Distribution of Radionuclides in the Peach Bottom HTGR Primary Circuit during Core 2 Operation," ERDA Report ORNL - 5188, Oak Ridge National Laboratory, to be published.

13. Hanson, D. L., General Atomic unpublished data, December 5, 1973.

14. Hanson, D. L., "Results of the General Atomic Deposition Loop Program," ERDA Report GA-A13140, General Atomic Company, April 1, 1976.

15. "HTGR Accident Initiation and Progression Analysis Status Report, Vol. 5, AIPA Fission Product Source Terms," ERDA Report GA-A13617, General Atomic Company, February 1976.

16. Craig, G. T., Consultant to General Atomic Company, private communication, September 23, 1975.

17. "HTGR Steam Generators, Peach Bottom Atomic Power Station, Design Report," Vol. I, C. F. Braun and Company.

18. Milstead, C. E., and L. R. Zumwalt, "Cesium Plateout on Stainless and Carbon Steels," USAEC Informal Report GAMD-7525, General Atomic, Division of General Dynamics, October 25, 1966.

19. Milstead, C. E., and L. R. Zumwalt, "Cesium Deposition on Stainless Steel," General Atomic Division of General Dynamics Report GA-7433, September 1, 1966.

20. "HTGR Fuels and Core Development Program Quarterly Progress Report for the Period Ending May 31, 1976," ERDA Report GA-A13941, General Atomic Company, June 30, 1976, Task 4.

21. Myers, B. F., and W. E. Bell, "Cesium Transport Data for HTGR Systems," ERDA Report GA-A13990, General Atomic Company, to be published.

22. Lister, D. H., "The Transport of Radioactive Corrosion Products in High-Temperature Water," Nucl. Sc., Eng. 58, 239 (1975).